Journal of the Brazilian Society of Mechanical Sciences and Engineering (2024) 46:212
https://doi.org/10.1007/s40430-024-04766-5

TECHNICAL PAPER

Multistability investigation for improved performance in a compact nonlinear energy harvester

Luã G. Costa[1] · Luciana L. S. Monteiro[2] · Marcelo A. Savi[1]

Received: 7 June 2023 / Accepted: 6 November 2023

Abstract
Nature provides abundant ambient mechanical energy in the form of vibration, sound, wave, wind, and biomechanical energy, which can be harvested to power electronic systems. Smart materials-based mechanical energy harvesting systems have attracted increasing attention over the past two decades due to their advantageous characteristics such as high power density, simple design, and scalability. Nevertheless, the design of compact and high-performing systems remains a challenge. This work deals with the analysis of a compact multistable dual-beam nonlinear energy harvester that can be configured for different stability layouts. By using a nonlinear dynamics analysis framework and suitable tools, a qualitative performance characterization of the harvester for each stability configuration is conducted. Results show that multistable characteristics associated with a softer inner beam characteristic and higher excitation levels are related to complex phenomena and can greatly enhance performance.

Keywords Energy harvesting · Smart materials · Nonlinear dynamics · Chaos · Compact structures · Multistability · Multiple DoF structures

1 Introduction

The increasing rate of development in contemporary society is causing an ecological imbalance in nature. The population growth and the technological advance associated with the increasing need for natural resources is expanding the society's energy demand and creating energy bottlenecks that need to be overcome. In this regard, the constant and rapidly evolution of electronic devices is enabling the reduction of their power consumption [35], however causing an increase in the production and propagation of e-waste due to the disposal of old hardware, including batteries. This scenario is pointing towards a critical planetary threshold. If crossed, it could irreversibly alter the environment as known [25]. This emphasizes the need to develop technology, to implement processes, and to change lifestyle having sustainability and renewability as the main philosophical pillars as a society.

This context has encouraged a surge of initiatives, research endeavors, and development efforts to shift away from the old paradigm and develop renewable and sustainable approaches that can ensure the continued reliability of our technology and processes [11]. In this regard, the harnessing of available environmental mechanical energy as vibration, wind, wave, sound, and biomechanical energy have become attractive as an alternative, sustainable and renewable power supply to completely replace traditional batteries or, at least, increase their lifespan [21].

The operating principle of the mechanical energy harvesters relies on transducer mechanisms that convert available mechanical energy into useful electrical energy. Electromagnetic induction [27], triboelectric structures [34], and smart materials such as piezoelectric ceramics [28], piezoelectric polymers [26], and magnetostrictive alloys [7] are the most conventional methods found in the literature. Hybrid strategies are also being employed to enhance the overall performance of mechanical energy harvesters, overcoming the limitations of the individual transduction methods [1, 12].

Technical Editor: Aline Souza de Paula.

✉ Marcelo A. Savi
savi@mecanica.coppe.ufrj.br

[1] Center for Nonlinear Mechanics, Universidade Federal do Rio de Janeiro, COPPE - Mechanical Engineering, Rio de Janeiro, RJ 21941-914, Brazil

[2] Centro Federal de Educação Tecnológica Celso Suckow da Fonseca, CEFET/RJ - Department of Mechanical Engineering, Rio de Janeiro 20.271.110, Brazil

Published online: 14 March 2024

The structural design configuration is another essential point to enhance energy harvesting capacity. In this regard, the cantilever structure, which employs slender beams as the main structural component, is a widely recognized, well documented, modeled and validated design for harvesters [10, 14, 15]. Nevertheless, this design suffers from a critical limitation, presenting a lack of efficiency when operating at frequencies that deviate from its natural frequency. Under these conditions, the deflection of the beam decreases, resulting in a low performance, hindering its application in practical circumstances.

Mechanical modulations have been proposed to improve the performance of the classical beam harvester. One interesting approach is the incorporation of degrees-of-freedom (DoF) to create a multimodal design that can operate efficiently in broadband spectrum [19]. From this perspective, Wu et al. [29] proposed a design comprising an outer and an inner beam. This design created a larger operating region, rendering the 2-DoF design a very compact construction with enhanced performance. Novel designs with geometry modifications have also demonstrated improved performance. Caetano and Savi [2] proposed a pizza-shaped system that exploited multiple DoF to achieve a broadband device, and later proposed a star-shaped device with coupled inertial masses that resulted in a broadband multidirectional energy harvester [3]. Similarly, Zhou et al. [31] introduced an arc-shaped geometry segment to the cantilever design, significantly enhancing its performance compared to the conventional design.

Nonlinear behavior is another essential point to be exploited to pursue more efficient designs. Countless nonlinear modulations have been proposed and continue to be explored [36]. These modifications have been found to significantly improve the performance of energy harvesters, especially in terms of broadband performance, making them attractive options for general applications. For example, the inclusion of magnetic interactions or mechanical buckling can create a multistability that creates additional stable conditions by inducing one or more regions of instability within the system. Multistable systems are effective as they have the potential to increase the deflections, enhancing its energy harvesting capabilities. Researchers have extensively investigated the capacity of multistability in one degree-of-freedom systems by exploring bistability [4, 18], tristability [16], tetrastability [33], and pentastability [32]. One of the main characteristic of multistable systems is the presence of a potential energy barrier that can reduce performance when low levels of input energy are available. Nonetheless, if the barriers are overcome, these systems can enhance both output power and bandwidth when compared to the classical linear systems [13]. Generally, evidence points that increasing the number of stable positions can shorten these energetic barriers and increase performance in low level excitation conditions, by the cost of increasing dynamical complexity [17].

Since the pioneer concepts of the usage of magnets [8, 24] and buckled structures [18, 23] to enhance the bandwidth of the classical linear harvesters, researchers have proposed and analyzed new forms of multistable systems, ranging from tristable to pentastable and beyond. Nevertheless, there is a lack of standard forms of comparison among the proposed systems and classical systems, coupled with biased reporting of results has made it difficult to differentiate good proposals from bad ones. Nonlinear dynamics perspective is an interesting approach to evaluate the energy harvesting capacity by considering different multistable aspects. On this basis, an objective and comprehensive evaluation of multistable systems can be performed, using the energy harvesting capacity as the main criterion.

This paper deals with a novel energy harvester that combines compactness, multistability, and multi-degree-of-freedoms by using an dual-beam structure, a pair of magnetic interactions, and two piezoelectric transducers attached to the main structure. This model was previously discussed in Costa and Savi [5] and is inspired in the original model proposed by Wu et al. [30] that considers a bistable system. This structure allows the analysis of different aspects of multistability, which is performed by investigating the nonlinear dynamics and performance of the energy harvesting system. This article expands a previous work by examining the qualitative effects of different magnetic configurations that define distinct stability states associated with magnetic setups [5]. Based on the excitation levels, the performance characteristics of each configuration are elucidated and compared, defining the best configuration for various operational scenarios, establishing a proper analysis of multistable aspects.

2 Design concept and theoretical model

A dual-beam compact energy harvesting system design is proposed based on the classical cantilever beam structure, presenting an inner–outer beam structure and nonlinear modulation based on magnetic interactions. This compact design maximizes the available space for high strain rates. Basically, an inner beam is incorporated into the outer beam, and each one of them has magnetic interactions and a piezoelectric transducer. This energy harvesting system is a compact multistable energy harvester of the same size as the conventional bistable energy harvester, but with potentially better performance capabilities as showed by Costa and Savi [5]. Figure 1 illustrates the design concept compared to the conventional bistable harvester. This design is more space-efficient and can offer better performance than the conventional version.

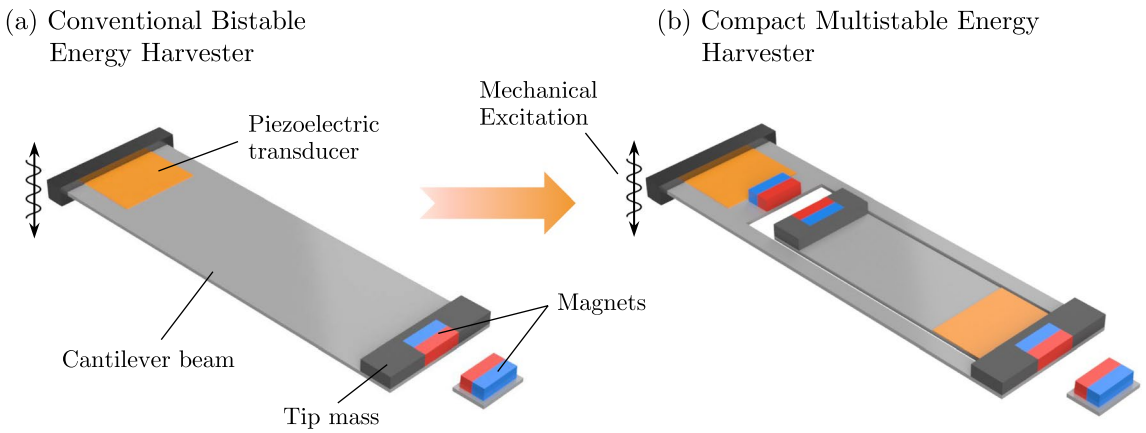

Fig. 1 Conceptual representation of the dual-beam nonlinear energy harvester, illustrating its compact and space-efficient design, which is comparable in size to the traditional bistable energy harvester

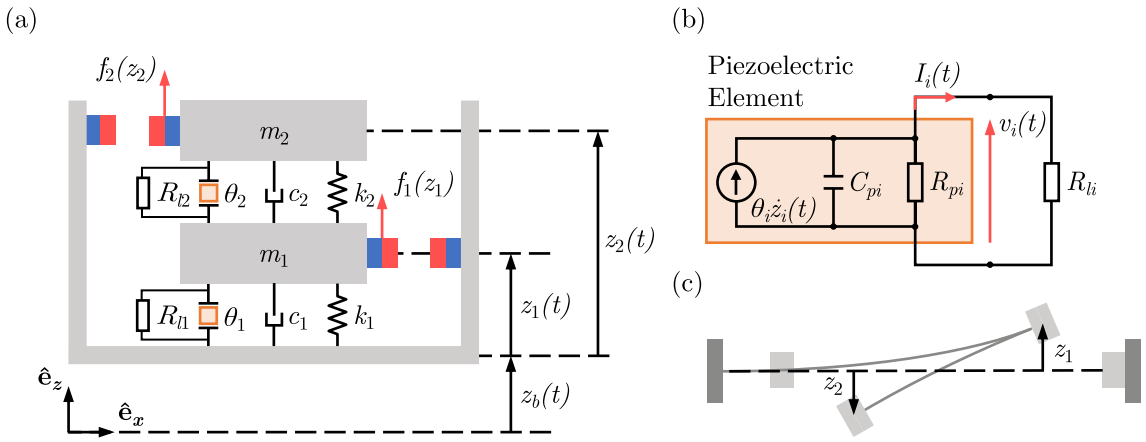

Fig. 2 Lumped model representing **a** the compact multistable energy harvester structure, **b** the equivalent electric circuit composed by the piezoelectric element attached to a resistance, and **c** the respective positive z directions for each DoF of the reduced order model related to the beam structure

2.1 Reduced order model

The proposed energy harvester is represented by a 2-degrees-of-freedom multistable reduced order prototype showed in Fig. 2. This archetype encompasses the main features of the energy harvester. In the prototype, the subscript $i = 1, 2$ represents the properties associated with each degree-of-freedom, such as the mass, m_i, the equivalent structural stiffness, k_i, and the equivalent dissipation coefficient c_i. Moreover, piezoelectric patches are attached to the structure, which can be modeled by the electromechanical coupling coefficient, θ_i, an equivalent internal capacitance, C_{pi}, and an internal resistance, R_{pi}.

The piezoelectric elements are connected to simple resistive circuits with load resistances, R_{li}, resulting in output voltages, $v_i(t)$. The equivalent electrical resistance of each circuit, R_i, is determined by the internal resistance of the piezoelectric element and the load resistance connected in parallel, so that $R_i = R_{\mathrm{li}}R_{\mathrm{pi}}/\left(R_{\mathrm{li}} + R_{\mathrm{pi}}\right)$. The equivalent circuit of each piezoelectric element is presented in Fig. 2b. The system is excited by a base motion with amplitude A_{b} and frequency ω, represented by $z_{\mathrm{b}} = A_{\mathrm{b}} \sin \omega t$. Furthermore, the displacement of each mass is represented by $z_i(t)$ and the respective positive directions related to the real harvester are represented in Fig. 2c, that is, when z_1 is positive, the motion of the outer beam is directed upward, while when z_2 is positive, the motion of the inner beam presents an downward direction. Also, the effects of gravity are neglected.

In its simplest manifestation, the constitutive relationship governing the magnetic interactions can be approximated by a polynomial restitution force function, $f_{\mathrm{m}}(x) = \mathrm{d}U_m(x)/\mathrm{d}x$, where $U_m(x)$ is the potential energy associated with the restitution force [6, 9, 17]. For a 1DoF symmetric multistable

Table 1 Common polynomial functions used to represent different symmetric stability conditions in a single-degree-of-freedom system

Stability	Magnetic restitution force, $f_{\mathrm{m}}(z)$	Magnetic potential energy, $U_m(z)$
1DoF bistable	$\mathfrak{a}_1 z - \mathfrak{a}_2 z^3$	$-\frac{1}{2}\mathfrak{a}_1 z^2 + \frac{1}{4}\mathfrak{a}_2 z^4$
1DoF tristable	$-\mathfrak{a}_1 z + \mathfrak{a}_2 z^3 - \mathfrak{a}_3 z^5$	$\frac{1}{2}\mathfrak{a}_1 z^2 - \frac{1}{4}\mathfrak{a}_2 z^4 + \frac{1}{6}\mathfrak{a}_3 z^6$
1DoF tetrastable	$\mathfrak{a}_1 z - \mathfrak{a}_2 z^3 + \mathfrak{a}_3 z^5 - \mathfrak{a}_4 z^7$	$-\frac{1}{2}\mathfrak{a}_1 z^2 + \frac{1}{4}\mathfrak{a}_2 z^4 - \frac{1}{6}\mathfrak{a}_3 z^6 + \frac{1}{8}\mathfrak{a}_4 z^8$

system with $N+1$ stable positions, these relationships can be expressed as follows:

$$f_{\mathrm{m}}(z) = \sum_{j=0}^{N} (-1)^{1+j+N} \mathfrak{a}_{j+1} z^{2j+1}, \tag{1}$$

$$U_m(z) = -\int_0^x f_{\mathrm{m}}(z)\mathrm{d}z = -\frac{1}{2}\sum_{j=0}^{N} (-1)^{1+j+N} \frac{1}{j+1} \mathfrak{a}_{j+1} z^{2(j+1)}. \tag{2}$$

Equations (1) and (2) provide a generalized representation of $f_{\mathrm{m}}(z)$ and $U_m(z)$, both of which require the inclusion of constant coefficients as essential input parameters $\mathfrak{a}_i, i = (1, \cdots, N)$. These input parameters represent the effect of the magnetic interactions and can be estimated by fitting the polynomial to experimental data [20]. In this regard, Table 1 provides a small compilation of common polynomial functions employed to represent distinct symmetric stability conditions within single-degree-of-freedom systems.

It is worth noting that these functions are for the magnetic interactions alone. The interplay between the equivalent structure's restitution force, denoted as $f_s(z)$, and the magnetic restitution force can have a significant impact on the system's stability condition. In the case of a single-degree-of-freedom system, this influence can alter the signal of the first term related to z[1]. For example, for a bistable system ($N = 1$), the resulting restitution force can be expressed as follows:

$$f(z) = f_{\mathrm{m}}(z) + f_{\mathrm{s}}(z) = \mathfrak{a}_1 z - \mathfrak{a}_2 z^3 - kz = (\mathfrak{a}_1 - k)z - \mathfrak{a}_2 z^3. \tag{3}$$

The bistability is associated with a positive coefficient preceding z, i.e., $(\mathfrak{a}_1 - k) > 0$. In systems with multiple degrees of freedom, these interactions become significantly more complex.

Within the context of the proposed system, one can apply this generalization in each degree-of-freedom separately. For a set with two magnets, a maximum of two stable equilibria arises at each DoF, implying that $N = 1$ should be used, resulting in Duffing-type restitution forces, and its respective potential energy functions of the form:

$$f_{\mathrm{m}_i}(z_i) = -a_i z_i(t) - b_i z_i(t)^3, \quad i = 1, 2; \tag{4}$$

$$U_m(z_1, z_2) = \sum_{i=1}^{2} \frac{1}{2} a_i z_i(t)^2 + \frac{1}{4} b_i z_i(t)^4, \tag{5}$$

where the coefficients $\mathfrak{a}_1 = a$ and $\mathfrak{a}_2 = b$, for better readability.

Under these assumptions, the determination of energy quantities are performed and the electromechanical equations are determined as follows[1]:

$$\begin{aligned} &m_1\ddot{z}_1 + c_1\dot{z}_1 - c_2\left(\dot{z}_2 - \dot{z}_1\right) + (k_1 + a_1)z_1 + b_1 z_1^3 \\ &\quad - k_2\left(z_2 - z_1\right) - \theta_1 v_1 + \theta_2 v_2 = -m_1\ddot{z}_b, \end{aligned} \tag{6}$$

$$\begin{aligned} &m_2\ddot{z}_2 + c_2\left(\dot{z}_2 - \dot{z}_1\right) + a_2 z_2 + b_2 z_2^3 \\ &\quad + k_2\left(z_2 - z_1\right) - \theta_2 v_2 = -m_2\ddot{z}_b, \end{aligned} \tag{7}$$

$$C_{p1}\dot{v}_1 + \frac{v_1}{R_1} + \theta_1\dot{z}_1 = 0, \tag{8}$$

$$C_{p2}\dot{v}_2 + \frac{v_2}{R_2} + \theta_2\left(\dot{z}_2 - \dot{z}_1\right) = 0. \tag{9}$$

To perform a qualitative analysis of these type of systems, a normalization approach is carried out by considering a reference length, L, and a reference voltage, V, resulting in the dimensionless electromechanical equations given by:

$$\begin{aligned} &\ddot{\bar{z}}_1 + 2\zeta_1\dot{\bar{z}}_1 - 2\zeta_2\left(\dot{\bar{z}}_2 - \dot{\bar{z}}_1\right) + \left(1 + \alpha_1\right)\bar{z}_1 + \beta_1\bar{z}_1^3 \\ &\quad - \rho\Omega_s^2\left(\bar{z}_2 - \bar{z}_1\right) - \chi_1\bar{v}_1 + \chi_2\bar{v}_2 = -\ddot{\bar{z}}_b, \end{aligned} \tag{10}$$

$$\begin{aligned} &\rho\ddot{\bar{z}}_2 + 2\zeta_2\left(\dot{\bar{z}}_2 - \dot{\bar{z}}_1\right) + \alpha_2\bar{z}_2 + \beta_2\bar{z}_2^3 + \rho\Omega_s^2\left(\bar{z}_2 - \bar{z}_1\right) \\ &\quad - \chi_2\bar{v}_2 = -\ddot{\bar{z}}_b, \end{aligned} \tag{11}$$

$$\dot{\bar{v}}_1 + \varphi_1\bar{v}_1 + \kappa_1\dot{\bar{z}}_1 = 0, \tag{12}$$

[1] From that point, the terms (t) and (τ) that indicates dependency of time are conveniently suppressed to write some expressions.

Table 2 System parameters and values used in the analyses. The values presented in this table are based on established literature sources [6, 9]

Parameter description	Symbol	Definition	Value
Linearized natural frequency of the 1st mass	ω_1	$\sqrt{k_1/m_1}$	–
Linearized natural frequency of the 2nd mass	ω_2	$\sqrt{k_2/m_2}$	–
Normalized time	τ	$\omega_1 t$	–
Normalized displacement of the 1st mass	$\bar{z}_1(\tau)$	$z_1(t)/L$	–
Normalized displacement of the 2nd mass	$\bar{z}_2(\tau)$	$z_2(t)/L$	–
Normalized voltage of the 1st circuit	$\bar{v}_1(\tau)$	$v_1(t)/V$	–
Normalized voltage of the 2nd circuit	$\bar{v}_2(\tau)$	$v_2(t)/V$	–
Normalized base excitation frequency	Ω	ω/ω_1	$0.01 \rightarrow 10$
Normalized base excitation amplitude	γ	A/L	$0.01 \rightarrow 1$
Normalized base excitation displacement	$\bar{z}_b(\tau)$	$\gamma \sin(\Omega\tau)$	–
Ratio of masses	ρ	m_2/m_1	1
Normalized mechanical damping coef. of the 1st mechanical DoF	ζ_1	$c_1/(2\omega_1 m_1)$	0.025
Normalized mechanical damping coef. of the 2nd mechanical DoF	ζ_2	$c_2/(2\omega_1 m_1)$	0.025
Ratio of linearized natural frequencies	Ω_s	ω_2/ω_1	$0.25 \rightarrow 2$
Normalized linear restitution coef. of the 1st mechanical DoF	α_1	$a_1/(\omega_1^2 m_1)$	$-2, 0, 1$
Normalized linear restitution coef. of the 2nd mechanical DoF	α_2	$a_2/(\omega_1^2 m_1)$	$-1, 0, 1$
Normalized nonlinear restitution coef. of the 1st mechanical DoF	β_1	$b_1 L^2/(\omega_1^2 m_1)$	1
Normalized nonlinear restitution coef. of the 2nd mechanical DoF	β_2	$b_2 L^2/(\omega_1^2 m_1)$	1
Normalized 1st piezoelectric coupling coef. in the mechanical ODE	χ_1	$\theta_1 V/(k_1 L)$	0.05
Normalized 2nd piezoelectric coupling coef. in the mechanical ODE	χ_2	$\theta_2 V/(k_1 L)$	0.05
Normalized 1st piezoelectric coupling coef. in the electrical ODE	κ_1	$\theta_1 L/(C_{p1} V)$	0.5
Normalized 2nd piezoelectric coupling coef. in the electrical ODE	κ_2	$\theta_2 L/(C_{p2} V)$	0.5
Normalized electrical conductance of the 1st circuit	φ_1	$1/(C_{p1} R_1 \omega_1)$	0.05
Normalized electrical conductance of the 2nd circuit	φ_2	$1/(C_{p2} R_2 \omega_1)$	0.05
Normalized output power of the 1st electrical DoF	$\bar{P}_1(\tau)$	$P_1(t)/(C_{p1}\omega_1 V^2)$	–
Normalized output power of the 2nd electrical DoF	$\bar{P}_2(\tau)$	$P_2(t)/(C_{p2}\omega_1 V^2)$	–

$$\dot{\bar{v}}_2 + \varphi_2 \bar{v}_2 + \kappa_2\left(\dot{\bar{z}}_2 - \dot{\bar{z}}_1\right) = 0, \tag{13}$$

that are related to dimensionless parameters presented in Table 2. For more formulation details refer to Costa and Savi [5].

The electromechanical system can be rewritten in its canonical form as follows:

$$\dot{\bar{\mathbf{q}}} = \mathbf{f}(\bar{\mathbf{q}}) = \begin{bmatrix} \dot{\bar{z}}_1 \\ -2\zeta_1\dot{\bar{z}}_1 + 2\zeta_2\left(\dot{\bar{z}}_2 - \dot{\bar{z}}_1\right) - \left(1+\alpha_1\right)\bar{z}_1 - \beta_1\bar{z}_1^3 + \rho\Omega_s^2\left(\bar{z}_2 - \bar{z}_1\right) + \chi_1\bar{v}_1 - \chi_2\bar{v}_2 - \ddot{\bar{z}}_b \\ \dot{\bar{z}}_2 \\ -\frac{1}{\rho}\left[2\zeta_2\left(\dot{\bar{z}}_2 - \dot{\bar{z}}_1\right) + \alpha_2\bar{z}_2 + \beta_2\bar{z}_2^3 - \chi_2\bar{v}_2\right] - \Omega_s^2\left(\bar{z}_2 - \bar{z}_1\right) - \ddot{\bar{z}}_b \\ -\varphi_1\bar{v}_1 - \kappa_1\dot{\bar{z}}_1 \\ -\varphi_2\bar{v}_2 - \kappa_2\left(\dot{\bar{z}}_2 - \dot{\bar{z}}_1\right) \end{bmatrix} \tag{14}$$

where $\bar{\mathbf{q}} = [\bar{z}_1(\tau), \dot{\bar{z}}_1(\tau), \bar{z}_2(\tau), \dot{\bar{z}}_2(\tau), \bar{v}_1(\tau), \bar{v}_2(\tau)]$.

2.2 Performance metrics

The performance analysis of the energy harvester device is usually defined by the electrical output variables. In this regard, either instantaneous or average values can be monitored. The instantaneous electrical power in a simple resistive circuit is commonly represented by Eq. (15). The average electrical power is represented by Eq. (16), where v_i^{RMS} are the root mean square of the output voltages.

$$P_i = \frac{1}{R_i} v_i^2, \tag{15}$$

$$P_{\text{avg}} = \sum_{i=1}^{2} \left[\frac{1}{t_f - t_0} \int_{t_0}^{t_f} P_i \, \mathrm{d}t \right] = \sum_{i=1}^{2} \left[\frac{1}{R_i} \left(v_i^{\text{RMS}} \right)^2 \right]. \tag{16}$$

Based on these concepts and according to Table 2, the normalized average electrical output power can be determined as follows:

$$\bar{P}_{\text{avg}} = \sum_{i=1}^{2} \left[\frac{1}{\tau_f - \tau_0} \int_{\tau_0}^{\tau_f} \bar{P}_i \, \mathrm{d}\tau \right] = \sum_{i=1}^{2} \left[\varphi_i \left(\bar{v}_i^{\text{RMS}} \right)^2 \right] \tag{17}$$

3 Multistable characteristics

The magnetic interactions within the system and the elastic properties of the structure have shown to be an interesting point to be investigated since they are directly related to the possible stability states, which are closely related to the enhancement of the energy harvesting capacity. The magnetic parameters (α_1, α_2, β_1 and β_2) represent the effects of magnetic fields defined by the magnet positioning within the system and its material properties, while the structure elastic properties are represented by the ratio between the structural stiffness of each DoF, $k_2/k_1 = \omega_2^2 m_2 / \left(\omega_1^2 m_1 \right) = \Omega_s^2 \rho$. For this analysis, Ω_s is chosen to represent the stiffness changes as both parameters, Ω_s and ρ can be used to that end. The value of $\rho = 1$ is assumed to be constant throughout all the analyses of this work.

The equilibrium configurations of the system can be determined by

$$\dot{\bar{\mathbf{q}}} = \mathbf{f}(\bar{\mathbf{q}}) = \mathbf{0}, \tag{18}$$

yielding a solution containing a group of sets of the form $\bar{\mathbf{q}} = \left\{ \bar{z}_1, \dot{\bar{z}}_1, \bar{z}_2, \dot{\bar{z}}_2, \bar{v}_1, \bar{v}_2 \right\}_j = \left\{ \bar{Z}_1, 0, \bar{Z}_2, 0, 0, 0 \right\}_j$ that determines each equilibrium position, where j determines the specific set within the solution. The nature of each equilibrium point can be determined through a linearization around each point, evaluating the Jacobian matrix, $\mathbf{J}$, that follows

$$\mathbf{J} = \nabla^{\mathrm{T}} \mathbf{f}(\bar{\mathbf{q}}) = \begin{bmatrix} 0 & 1 & 0 & 0 & 0 & 0 \\ -1 - \alpha_1 - \rho\Omega_s^2 - 3\beta_1 \bar{z}_1^2 & -2\left(\zeta_1 + \zeta_2\right) & \rho\Omega_s^2 & 2\zeta_2 & \chi_1 & -\chi_2 \\ 0 & 0 & 0 & 1 & 0 & 0 \\ \Omega_s^2 & \dfrac{2\zeta_2}{\rho} & -\dfrac{\alpha_2 + \rho\Omega_s^2 + 3\beta_2 \bar{z}_2^2}{\rho} & -\dfrac{2\zeta_2}{\rho} & 0 & \dfrac{\chi_2}{\rho} \\ 0 & -\kappa_1 & 0 & 0 & -\varphi_1 & 0 \\ 0 & \kappa_2 & 0 & -\kappa_2 & 0 & -\varphi_2 \end{bmatrix} \tag{19}$$

The stability characteristics of each point is evaluated from the eigenvalues, μ, of the Jacobian matrix. These points can be classified into three sets: (1) stable if $\left\{ \mu_k \in \mathbb{C} \mid \mathrm{Re}\left(\mu_k\right) < 0 \right\}$, (2) Unstable if $\left\{ \mu_k \in \mathbb{C} \mid \mathrm{Re}\left(\mu_k\right) > 0 \right\}$, and (3) Center if $\left\{ \mu_k \in \mathbb{C} \mid \mathrm{Re}\left(\mu_k\right) = 0 \right\}$. Besides that, the stability of the linearized system at the vicinity of an equilibrium point corresponds to the nonlinear system as long as the point is hyperbolic, meaning that all the eigenvalues have a non-null real part $\left(\mathrm{Re}\left(\mu_k\right) \neq 0, \forall k\right)$ [22].

On this basis, all solutions are hyperbolic and the unstable points can be split into two distinct groups: saddle-type unstable points and source-type unstable points. Saddle-type unstable points exhibit one positive eigenvalue, indicating the characteristic of a single unstable direction. On the other hand, source-type unstable points exhibit two positive eigenvalues, indicating the characteristic of two unstable directions. Additionally, the stability analysis can be further complemented by evaluating the normalized form of the potential energy function, as detailed in Eq. (20), and sections of the basins of attraction of the non-forced system, providing a comprehensive understanding of the system's stability characteristics.

$$\bar{U} = \frac{1}{2}\left(1 + \alpha_1\right)\bar{z}_1^2 + \frac{1}{4}\beta_1 \bar{z}_1^4 + \frac{1}{2}\rho\Omega_s^2 \left(\bar{z}_2 - \bar{z}_1\right)^2 + \frac{1}{2}\alpha_2 \bar{z}_2^2 + \frac{1}{4}\beta_2 \bar{z}_2^4 \tag{20}$$

The solution sets $\left\{ \bar{z}_1, \dot{\bar{z}}_1, \bar{z}_2, \dot{\bar{z}}_2, \bar{v}_1, \bar{v}_2 \right\}_j = \left\{ \bar{Z}_1, 0, \bar{Z}_2, 0, 0, 0 \right\}_j$ allow the visualization of stability characteristics through the subsets $\left\{ \bar{z}_1, \bar{z}_2 \right\}_j = \left\{ \bar{Z}_1, \bar{Z}_2 \right\}_j$, as the other values are zero and do not change. From this point forward, the term "basin of attraction" will be used as a shorthand to the expression "section of the basin of attraction", as the basin of attraction of the system has 6 dimensions, while the analysis is reduced to a section of the basin with 2 dimensions. The result of the stability analysis is summarized in Figs. 3, 4, 5 and 6. Each figure represents a different configuration defined by a set of values for the magnetic restitution parameters α_1, α_2, β_1 and β_2. In each case, the stability state is determined for different values of Ω_s. In the first row (letters a, b, c and d) the potential energy levels are associated with the equilibrium positions and its vicinity. The colorbar represents the potential

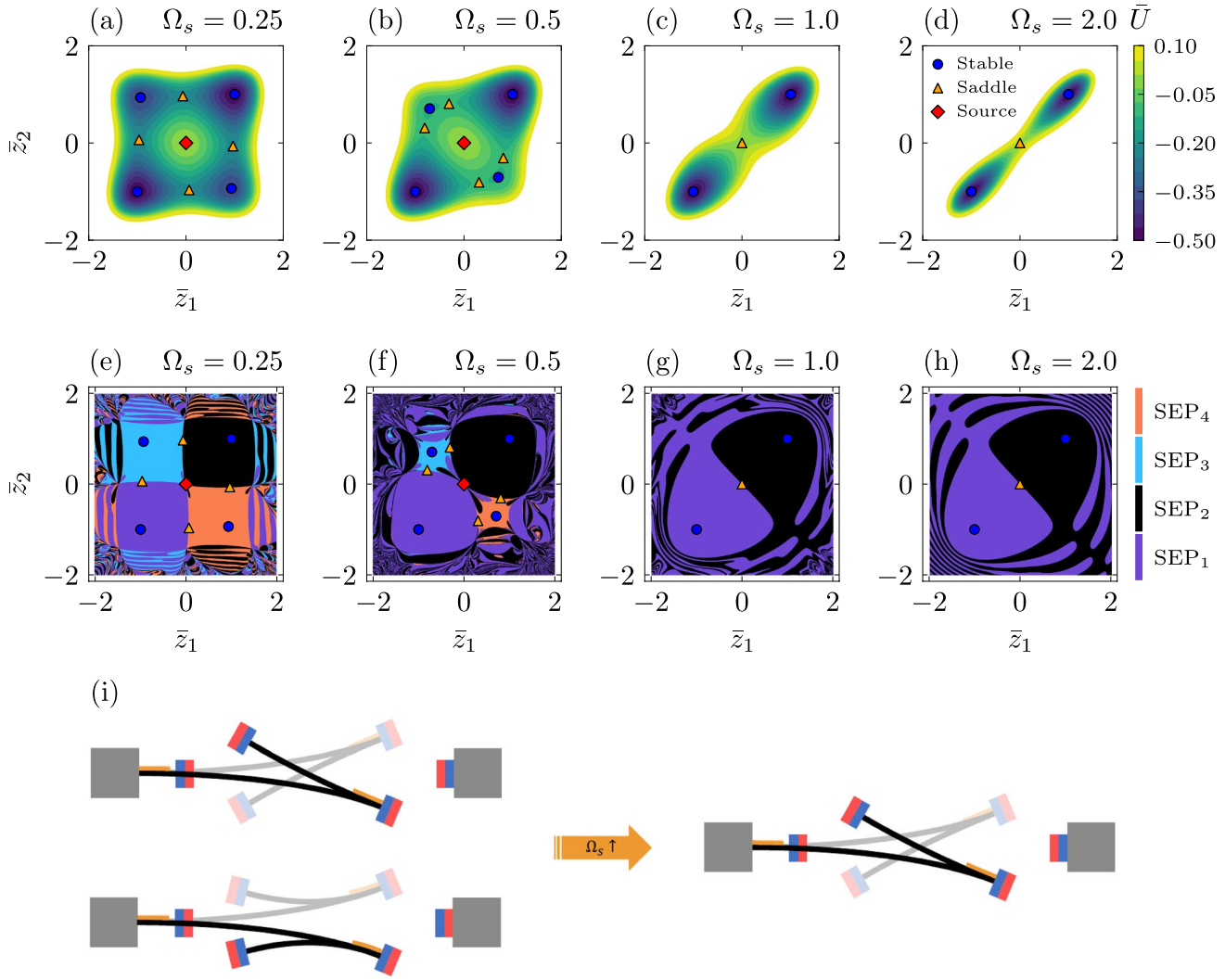

Fig. 3 Equilibrium configurations for a set of Ω_s values, considering the magnetic configuration represented by the coefficients $(\alpha_1, \alpha_2, \beta_1, \beta_2) = (-2, -1, 1, 1)$ and a fix mass ratio of $\rho = 1$. The first row represent the potential energy levels for each configuration **a** for $\Omega_s = 0.25$, **b** for $\Omega_s = 0.5$, **c** for $\Omega_s = 1$, and **d** for $\Omega_s = 2$. The colorbar indicates the level of potential energy for each combination of system positions $\bar{z}_1$ and $\bar{z}_2$. The second row represents the evolution of the basins of attraction for each configuration **e** for $\Omega_s = 0.25$, **f** for $\Omega_s = 0.5$, **g** for $\Omega_s = 1$, and (h) for $\Omega_s = 2$, where each color represents the stable equilibrium position the system converges to if released from an initial condition within the $\bar{z}_1 \times \bar{z}_2$ parameter domain. The equilibrium position associated with each colored region is the one located within the largest region of that specific color. A grid of 2000×2000 points is used for each basin. In both rows, blue dots represent stable equilibrium positions, orange triangles represent unstable saddle-type equilibrium positions and red polygons represent unstable source-type equilibrium positions. **i** Represents one of the possible representations of the stable equilibrium states as Ω_s increases for this set of restitution parameters

energy levels, with darker colors representing lower energies and lighter colors representing higher energies. The second row (letters e, f, g and h) shows the basins of attraction plotted using up to four colors to indicate the stable attractors, which are the stable equilibrium points ($\text{SEP}_i, i = 1, \ldots, 4$) where the system converges if released from the initial conditions within the domain $\bar{z}_1 \times \bar{z}_2$, where $\bar{z}_1 \in [-2, 2]$ and $\bar{z}_2 \in [-2, 2]$, and $\dot{\bar{z}}_1 = \dot{\bar{z}}_2 = \bar{v}_1 = \bar{v}_2 = 0$. In both rows, blue dots indicate stable equilibria, orange triangles indicate unstable saddle-type equilibria, and red polygons (diamonds) indicate unstable source-type equilibria. Also, for each case, the stability plots are followed by a possible representation of the initial and final stable equilibrium states, related to the beam structure, as Ω_s increases (letter i).

Figure 3 displays a case with $(\alpha_1, \alpha_2, \beta_1, \beta_2) = (-2, -1, 1, 1)$, related to the configuration represented in Fig. 3i where the two sets of magnets are set up in repulsive mode.

In this case, for low values of $\Omega_s < 0.5$, that is, when the inner beam is softer than the outer beam, the system exhibit 9 equilibrium positions, being 4 of them stable and 5 unstable, which means that a tetrastable system is of concern. By increasing the stiffness of the inner beam with respect

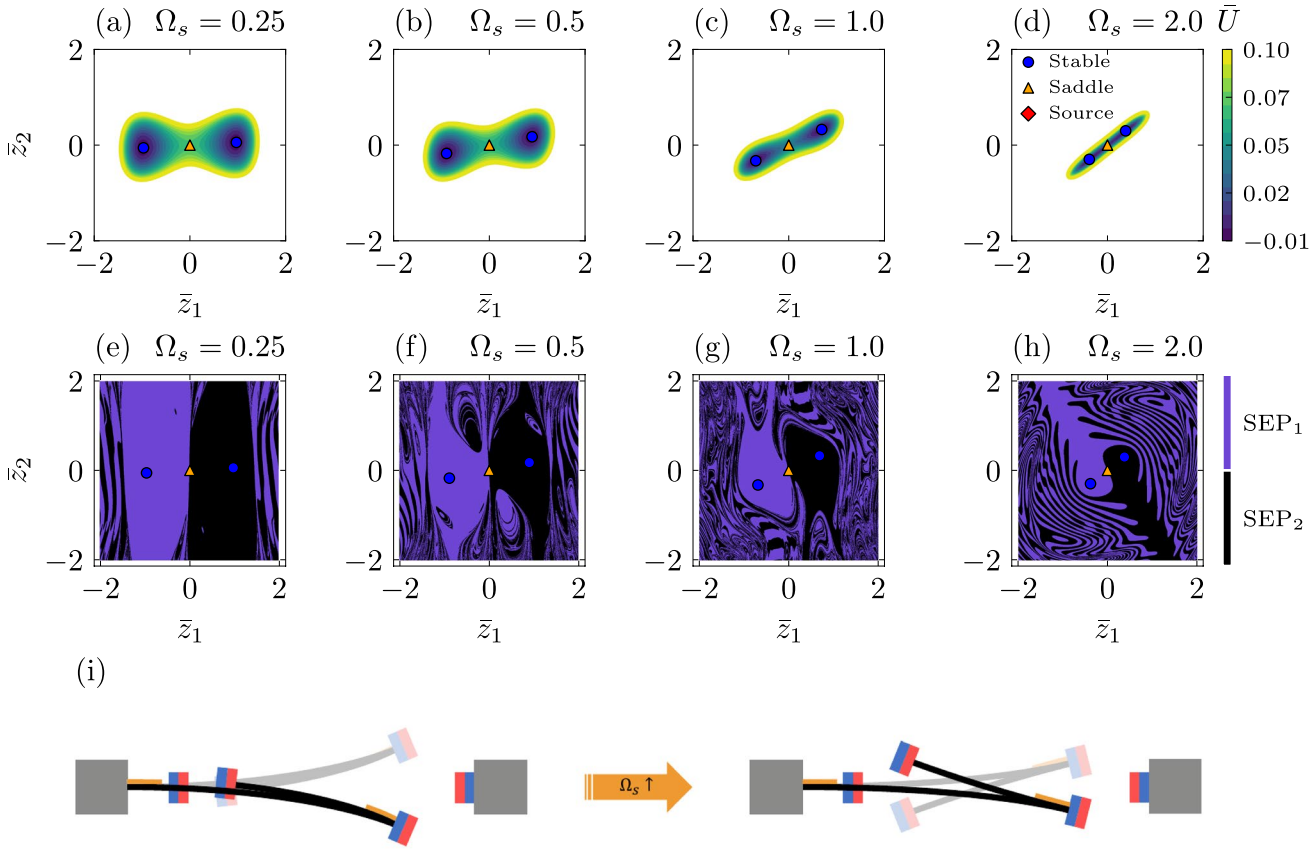

Fig. 4 Equilibrium configurations for a set of Ω_s values, considering the magnetic configuration represented by the coefficients $(\alpha_1, \alpha_2, \beta_1, \beta_2) = (-2, 1, 1, 1)$ and a fix mass ratio of $\rho = 1$. The first row represent the potential energy levels for each configuration **a** for $\Omega_s = 0.25$, **b** for $\Omega_s = 0.5$, **c** for $\Omega_s = 1$, and **d** for $\Omega_s = 2$. The colorbar indicates the level of potential energy for each combination of system positions $\bar{z}_1$ and $\bar{z}_2$. The second row represents the evolution of the basins of attraction for each configuration **e** for $\Omega_s = 0.25$, **f** for $\Omega_s = 0.5$, **g** for $\Omega_s = 1$, and **h** for $\Omega_s = 2$, where each color represents the stable equilibrium position the system converges to if released from an initial condition within the $\bar{z}_1 \times \bar{z}_2$ parameter domain. The equilibrium position associated with each colored region is the one located within the largest region of that specific color. A grid of 2000×2000 points is used for each basin. In both rows, blue dots represent stable equilibrium positions, orange triangles represent unstable saddle-type equilibrium positions and red polygons represent unstable source-type equilibrium positions. **i** Represents one of the possible representations of the stable equilibrium states as Ω_s increases for this set of restitution parameters

to the outer beam, the structure's restitution force becomes stronger than the magnetic force, eliminating 6 equilibrium positions, resulting in a bistable configuration with 2 stable equilibrium positions and 1 unstable.

Figure 4 shows a case with $(\alpha_1, \alpha_2, \beta_1, \beta_2) = (-2, 1, 1, 1)$. In this case, for all values of Ω_s the system remains in bistable mode. A possible representation of this case is presented in Fig. 4e, where the set of magnets attached to the outer beam remains in repulsive mode, while the set of magnets related to the inner beam is set up to attractive mode. With a softer inner beam, it tends to retain the position of the inner beam close to zero as the magnetic force is stronger than the inner beam structure's restitution force. By increasing Ω_s, the enhancement in inner beam stiffness tends to increase the distance of its equilibrium position with respect to the neutral axis, while reducing the distance of the outer beam equilibrium position. Another possible representation of this case can retain the repulsive mode of the inner beam, but with an increased distance between the magnets, sufficient to not induce a change in stability of the inner beam, and remaining with the nonlinear characteristics. The final state of this configuration, represented in Fig. 4d, is similar to the one showed in Fig. 3d, but with a shorter distance between stable equilibrium positions.

Figure 5 represent a case with $(\alpha_1, \alpha_2, \beta_1, \beta_2) = (0, -1, 1, 1)$ $(\alpha_1, \alpha_2, \beta_1, \beta_2) = (0, -1, 1, 1)$. This case also consists in a bistable characteristic for all values of Ω_s analyzed. A possible representation for this configuration is presented in Fig. 5e where the magnets related to the outer beam are set up in attractive mode; while, the magnets of the inner beam are arranged in repulsive mode. Similar to the previous case, for a softer inner beam, it presents a higher amplitude than the

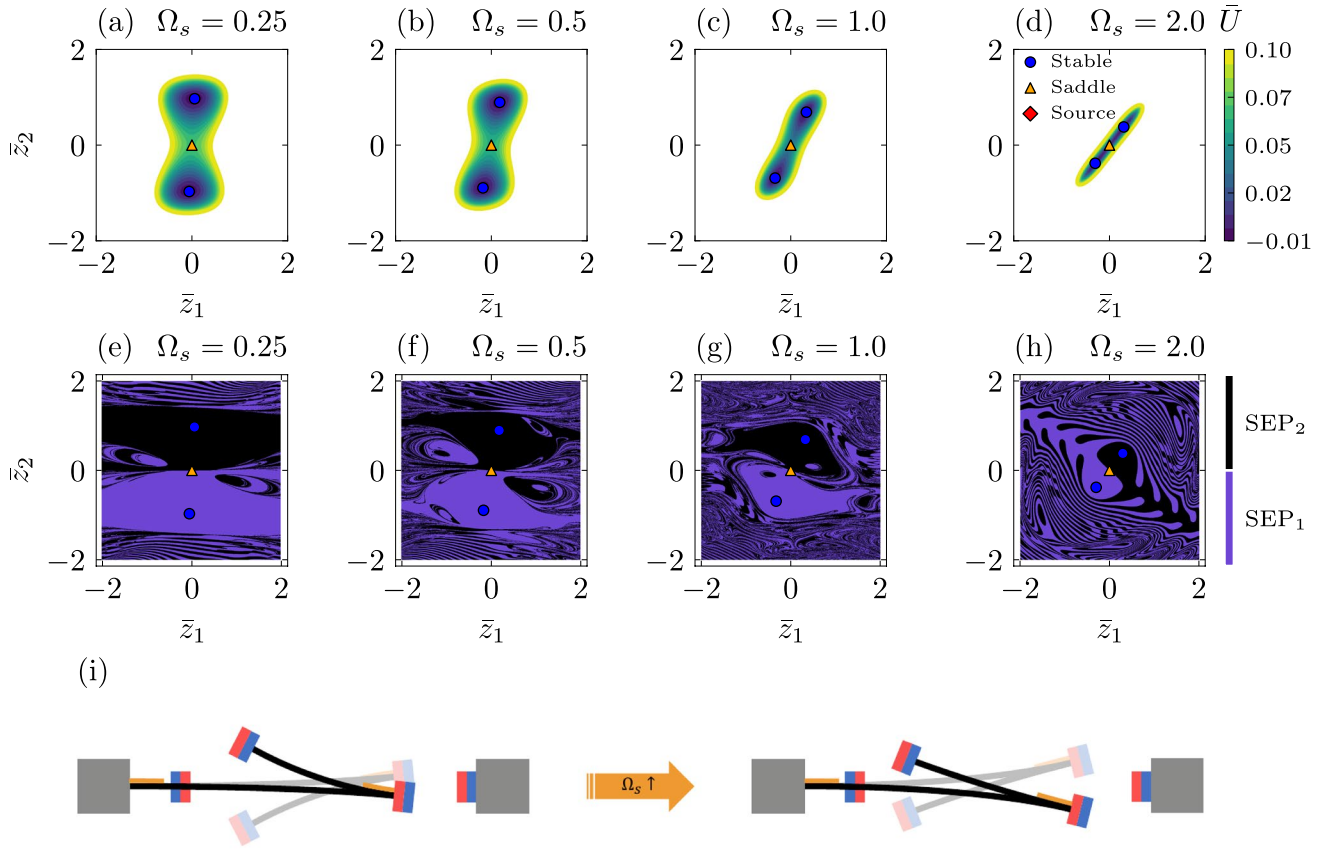

Fig. 5 Equilibrium configurations for a set of Ω_s values, considering the magnetic configuration represented by the coefficients $(\alpha_1, \alpha_2, \beta_1, \beta_2) = (0, -1, 1, 1)$ and a fix mass ratio of $\rho = 1$. The first row represent the potential energy levels for each configuration **a** for $\Omega_s = 0.25$, **b** for $\Omega_s = 0.5$, **c** for $\Omega_s = 1$, and **d** for $\Omega_s = 2$. The colorbar indicates the level of potential energy for each combination of system positions $\bar{z}_1$ and $\bar{z}_2$. The second row represents the evolution of the basins of attraction for each configuration **e** for $\Omega_s = 0.25$, **f** for $\Omega_s = 0.5$, **g** for $\Omega_s = 1$, and **h** for $\Omega_s = 2$, where each color represents the stable equilibrium position the system converges to if released from an initial condition within the $\bar{z}_1 \times \bar{z}_2$ parameter domain. The equilibrium position associated with each colored region is the one located within the largest region of that specific color. A grid of 2000×2000 points is used for each basin. In both rows, blue dots represent stable equilibrium positions, orange triangles represent unstable saddle-type equilibrium positions and red polygons represent unstable source-type equilibrium positions. **i** Represents one of the possible representations of the stable equilibrium states as Ω_s increases for this set of restitution parameters

outer beam. The force transmitted by the repulsive magnets to the beam structure cause a small deflection in the outer beam, translating its equilibrium position off the neutral axis. By increasing Ω_s, the stiffness of the inner beam increases, leading to an increase in the deflection of the outer beam, and a reduction in the reflection of the inner beam. Another representation of this state can retain the repulsive characteristics of the outer beam's magnets, but with increased distance between them. This would retain the nonlinear characteristics but the forces between the magnets would not be sufficient to induce more equilibrium positions. The final state of this configuration, represented in Fig. 5d, is similar to the final state configuration of the previous case, as showed in Fig. 4d.

The last equilibrium state found is depicted in Fig. 6. In this case, the system presents monostable characteristics for all values of Ω_s. Possible representations of this state comprises of the two sets of magnets set up in attractive mode or in repulsive mode, but with an increased distance between magnets to make the magnetic interactions weak, remaining nonlinear.

4 Energy harvesting performance characteristics

In this section, the performance characteristics of the system are of concern. Based on the conclusions of the stability analysis, eight configurations with different magnetic and structural parameters are chosen and labeled, being summarized in Table 3. For each set of magnetic arrangements, two values of Ω_s are chosen (0.25 and 1), enabling a general overview of the system's performance across each set of magnetic restitution parameters. Furthermore, the analysis is

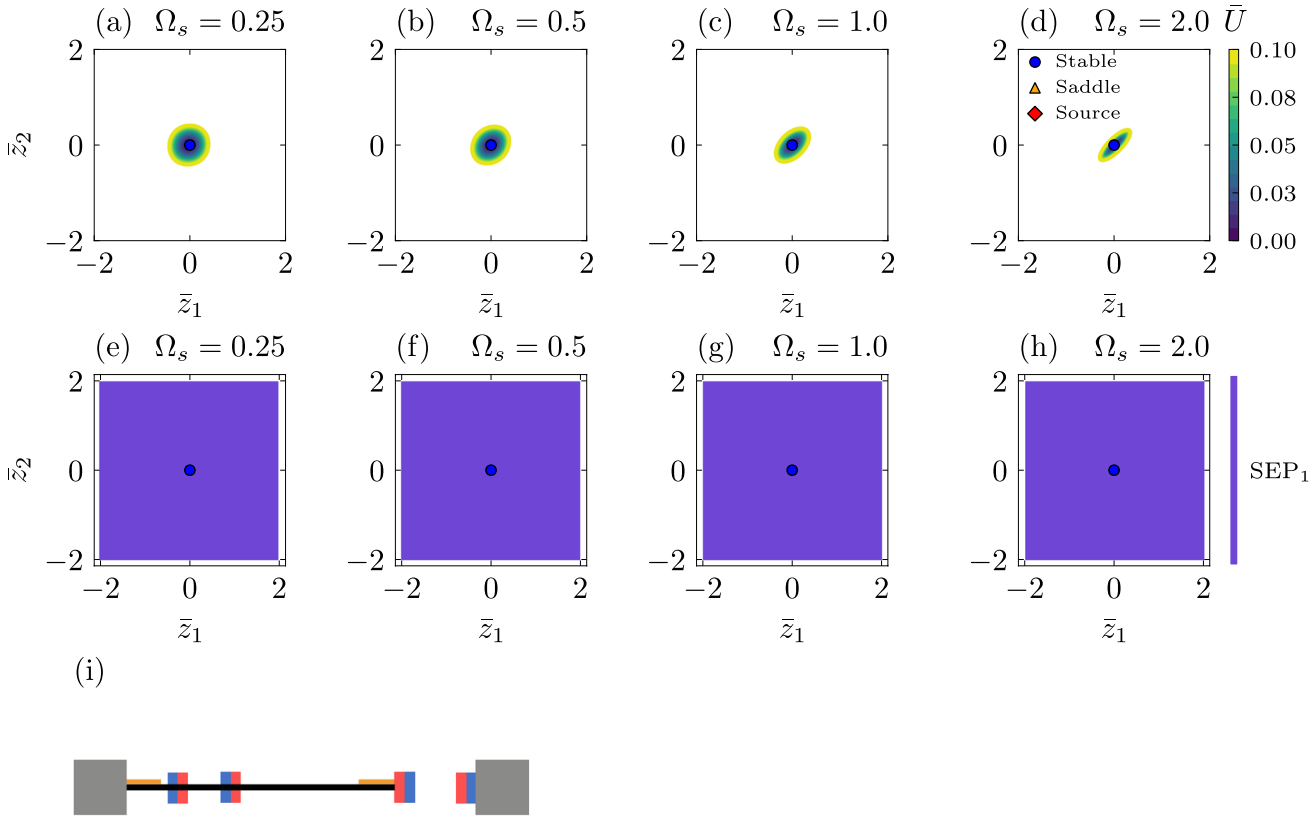

Fig. 6 Equilibrium configurations for a set of Ω_s values, considering the magnetic configuration represented by the coefficients $(\alpha_1, \alpha_2, \beta_1, \beta_2) = (0, 1, 1, 1)$ and a fix mass ratio of $\rho = 1$. The first row represent the potential energy levels for each configuration **a** for $\Omega_s = 0.25$, **b** for $\Omega_s = 0.5$, **c** for $\Omega_s = 1$, and **d** for $\Omega_s = 2$. The colorbar indicates the level of potential energy for each combination of system positions $\bar{z}_1$ and $\bar{z}_2$. The second row represents the evolution of the basins of attraction for each configuration **e** for $\Omega_s = 0.25$, **f** for $\Omega_s = 0.5$, **g** for $\Omega_s = 1$, and **h** for $\Omega_s = 2$, where each color represents the stable equilibrium position the system converges to if released from an initial condition within the $\bar{z}_1 \times \bar{z}_2$ parameter domain. The equilibrium position associated with each colored region is the one located within the largest region of that specific color. A grid of 2000×2000 points is used for each basin. In both rows, blue dots represent stable equilibrium positions, orange triangles represent unstable saddle-type equilibrium positions and red polygons represent unstable source-type equilibrium positions. **i** Represents one of the possible representations of the stable equilibrium states as Ω_s increases for this set of restitution parameters

Table 3 Stability configurations based on the combination of different magnetic and structural parameters

Magnetic				Structural		Stability	Configuration
α_1	α_2	β_1	β_2	ρ	Ω_s		
−2	−1	1	1	1	0.25	Tetrastable	I
					1	Bistable	II
−2	1	1	1	1	0.25	Bistable	III
					1	Bistable	IV
0	−1	1	1	1	0.25	Bistable	V
					1	Bistable	VI
0	1	1	1	1	0.25	Monostable	VII
					1	Monostable	VIII

divided into two aspects, considering lower and higher levels of input mechanical excitation amplitude, γ.

A normalized harmonic excitation displacement of the form $\bar{z}_b = \gamma \sin(\Omega\tau)$ is chosen to represent the available

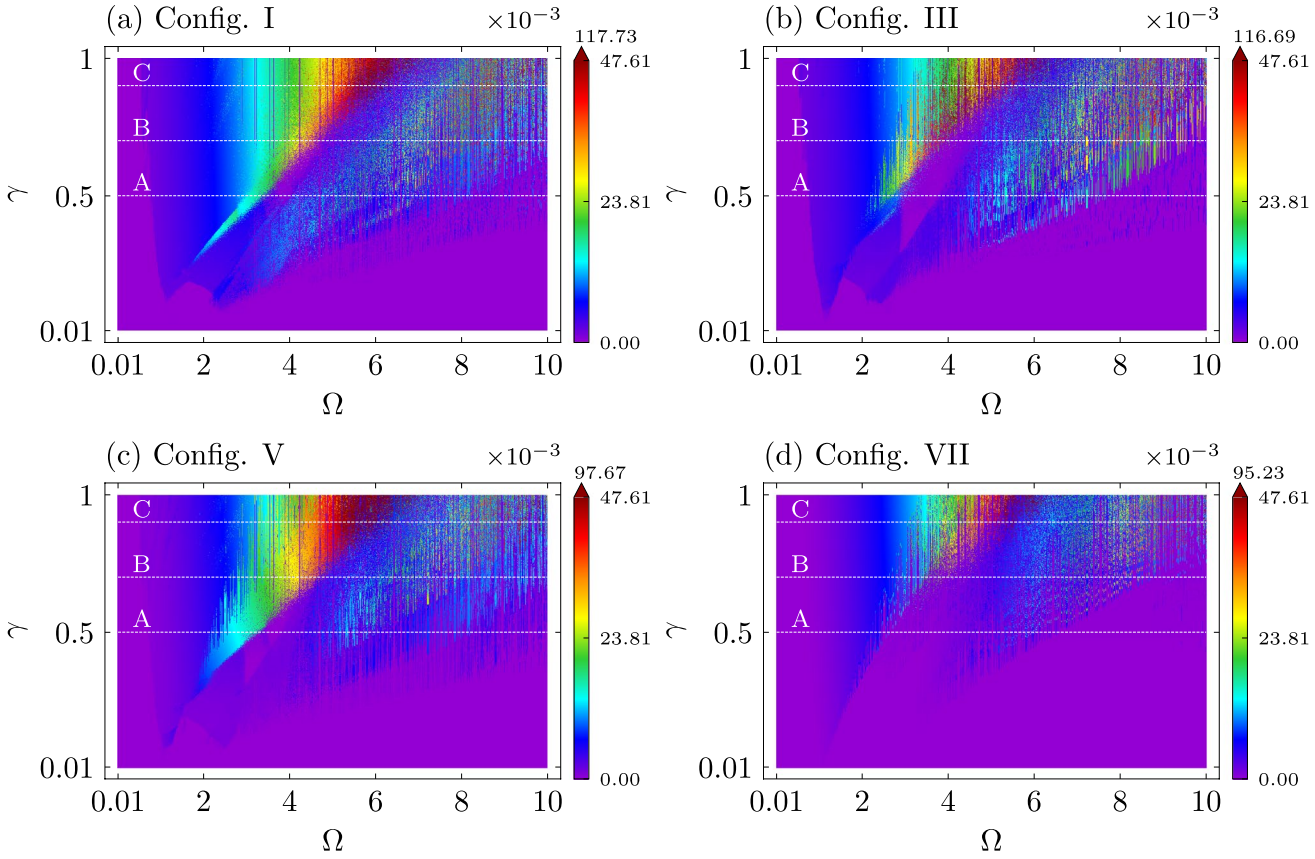

Fig. 7 Average output power diagrams (OPDs) for the configurations related to $\Omega_s = 0.25$. The colorbars represent the average output power levels for each excitation condition. To facilitate the interpretation, the range of each colorbar is restricted to a limit value, with the uppermost value of the colorbar on the peak of the colorbar arrow representing the maximum output power obtained by the harvester. All output power values are multiplied by 10^{-3}. White lines with capital letter labels are discussed in text and are represented by the frequency response diagrams in Fig. 8

environmental mechanical energy, where γ and Ω denote the excitation amplitude and frequency, respectively. Numerical investigations are performed by means of average output power diagrams (OPDs) that shows the steady state average electrical output power under the applied excitation $\bar{z}_b$ within the $\gamma \times \Omega$ parameter domain. The diagrams are built with a grid of 1000×1000 sample points, each of which is obtained from a time series from numerical integration employing the fourth-order Runge–Kutta method considering time steps $\Delta\tau \propto (T = 2\pi/\Omega)$. For each sample point, 4000 excitation periods ($4000T$) are imposed, with the last 500 considered to be the steady state, that is, when $\tau \geq 0.875\tau_f$; τ_f denotes the final time of integration. The initial conditions for each point on the diagrams are based on the stable position $\left\{\bar{z}_1, \dot{\bar{z}}_1, \bar{z}_2, \dot{\bar{z}}_2, \bar{v}_1, \bar{v}_2\right\} = \left\{\bar{Z}_1, 0, \bar{Z}_2, 0, 0, 0\right\}$ represented by the black basin of attraction (SEP_2) for the configurations I to VI at $\Omega_s = 0.25$, and the only existing stable position for the configurations VII and VIII. By utilizing these diagrams, a comprehensive overview of the qualitative performance characteristics of the system under different excitation conditions is presented.

4.1 Performance at high-amplitude mechanical excitation

Figure 7 depicts the OPDs for the configurations with $\Omega_s = 0.25$, as described in Table 3. The colorbars accompanying each diagram represent the average output power levels, restricted to a specific limit value to facilitate interpretation. The uppermost values indicated by the peak of the colorbar arrow represent the maximum normalized output power achieved by the harvester. By examining the OPDs at higher excitation amplitudes ($\gamma \geq 0.5$), it is evident that configurations I and III outperform the others for lower frequencies ($0.01 \leq \Omega < 3$). These configurations exhibit larger regions characterized by good output power values, represented by shades of blue. Moreover, configurations I and V demonstrate larger regions associated with very high output power (shades of red) for mid-range frequencies. It should be noted that, in these regions, configuration III displays shorter, scattered regions of very high performance, primarily related to the presence of distinct attractors associated with low and high performance, as previously discussed by

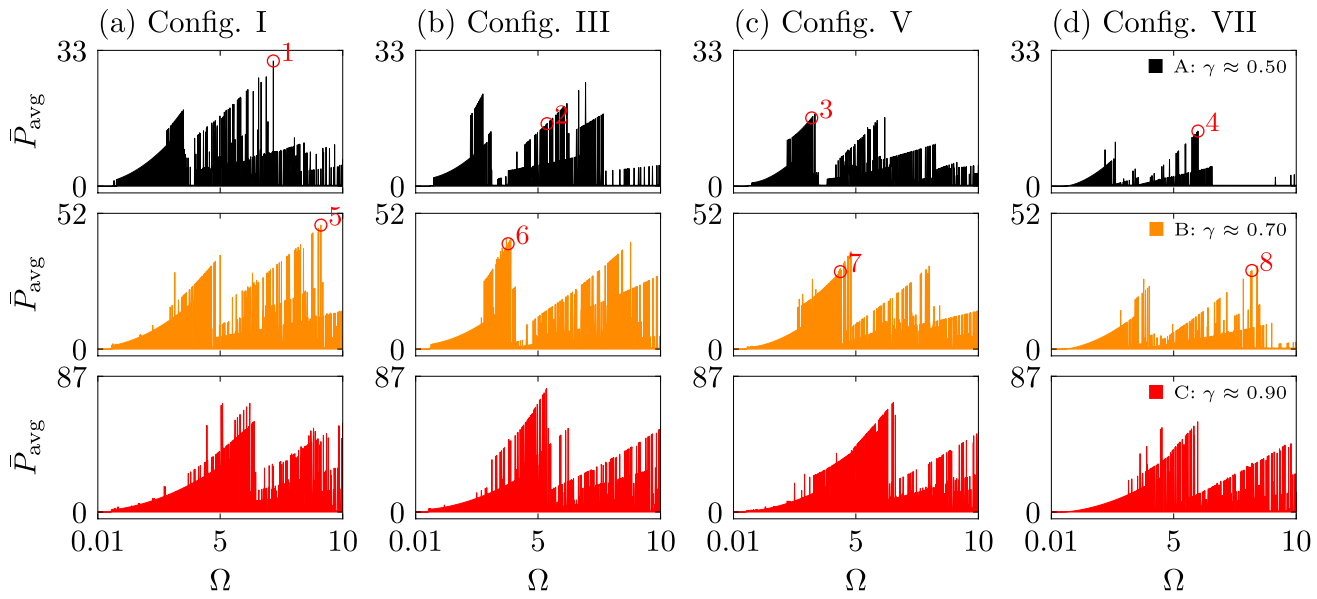

Fig. 8 Average output power for different values of constant γ. Each level of γ is highlighted by a different color: black for $\gamma \approx 0.5$, orange for $\gamma \approx 0.7$ and red for $\gamma \approx 0.9$. The constant values of γ are represented in Fig. 7 by the labels A, B and C. All average output power values are multiplied by 10^{-3}

Costa and Savi [5]. Nonetheless, configuration III shows small regions of superior performance at lower γ values ($0.5 \leq \gamma \leq 0.6$) when compared to configurations I and V.

In the case of higher frequencies ($7 \leq \Omega \leq 10$), almost all regions observed are predominantly associated with the presence of multiple dynamical attractors. This type of phenomenon is further explored in Sect. 4.3. Notably, configuration III exhibits superior performance in these scenarios. Conversely, configuration VII consistently demonstrates the worst performance across all examined scenarios.

These findings can be further illustrated in Fig. 8, which provides a visual representation of the output power for constant values of γ, denoted as A ($\gamma \approx 0.5$), B ($\gamma \approx 0.7$) and C ($\gamma \approx 0.9$) in each OPD presented in Fig. 7. Notably, configuration I, characterized by tetrastability, demonstrates superior performance in terms of both bandwidth and maximum output power for $\gamma \approx 0.5$ and $\gamma \approx 0.7$. Conversely, configurations III and V, associated with bistability, exhibit similar performance characteristics, while configuration VII, associated with monostability, consistently displays the poorest performance. Furthermore, for values $\gamma \approx 0.9$, all configurations demonstrate comparable performance, although configuration VII exhibits a slightly lower maximum output power when compared to the other configurations.

Details about each kind of behavior can be observed in Figs. 9 and 10 that present phase subspaces $\bar{z}_1 \times \dot{\bar{z}}_1$, $\bar{z}_2 \times \dot{\bar{z}}_2$, and $\bar{z}_1 \times \bar{z}_2$ of points 1 to 8 situated at the vicinity of maximum output power values in Fig. 8. Equilibrium points of the corresponding configuration in the $\bar{z}_1 \times \bar{z}_2$ are also displayed for spatial reference. These figures offer insights into the type of motion that leads to high performance under high-amplitude excitation. Essentially, the eight cases can be categorized into two sets based on the shape of the orbits. The 1T gray orbits of high performance are found at intermediary values of frequency; while, the 3T orbits of high performance are found at higher values of frequency.

Figure 11 depicts the performance analysis for different configurations of the harvester with $\Omega_s = 1$, as showed in Table 3, considering values of $\gamma \geq 0.5$. In this scenario, the careful observation of the OPDs points at a greater overall bandwidth and maximum output power for the configuration II. Configurations IV and VI present very similar performance to each other, and configuration VIII displays the worst performance. In a supplementary manner, Fig. 12 shows that the difference in performance between configurations II and configurations IV and VI is reduced as γ increases. Nevertheless, configuration VIII, associated with monostability, displays the worst performance.

Overall, this subsection demonstrates that in scenarios with higher amplitude excitations ($\gamma \geq 0.5$), the configurations associated with the magnetic parameters $(\alpha_1, \alpha_2, \beta_1, \beta_2) = (-2, -1, 1, 1)$ exhibit superior performance. Conversely, configurations associated with monostability consistently display the worst performance.

4.2 Performance at low amplitude mechanical excitation

Henceforth, the performance associated with lower amplitude excitation scenarios are of concern. Costa and Savi [5] had established that that lower excitation amplitudes coupled with higher excitation frequencies results in negligible

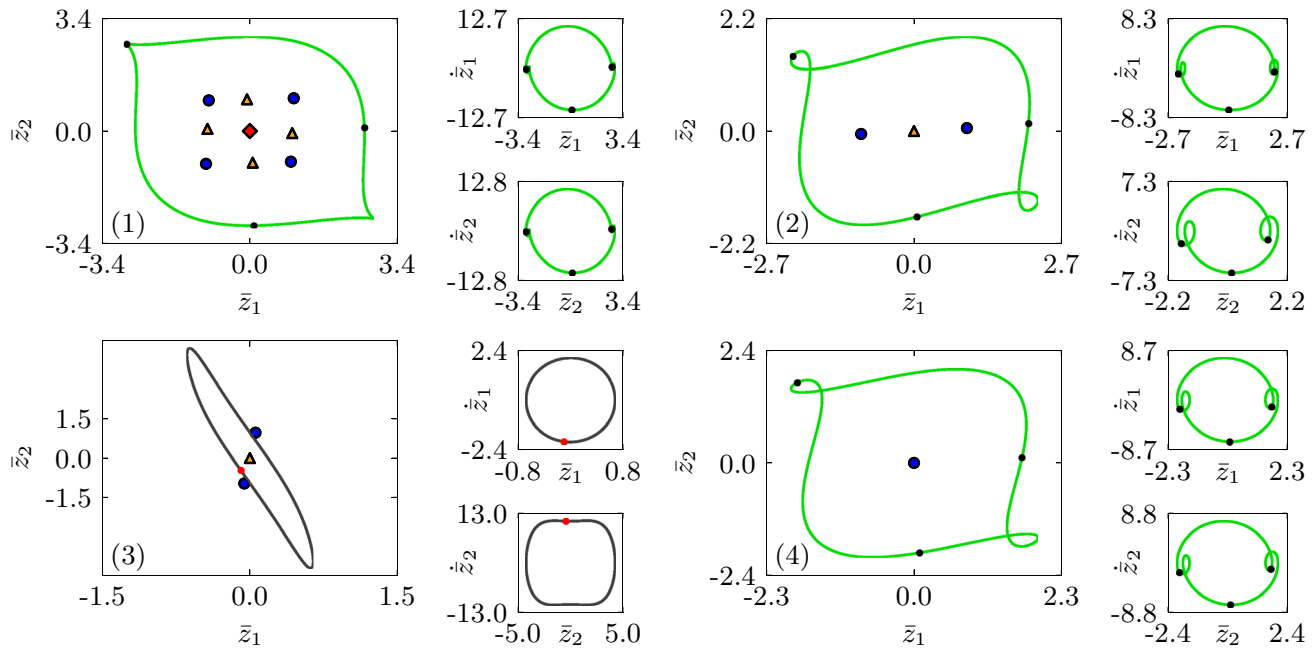

Fig. 9 Phase subspaces $\bar{z}_1 \times \bar{z}_2$, $\bar{z}_1 \times \dot{\bar{z}}_1$ and $\bar{z}_2 \times \dot{\bar{z}}_2$ of the steady state response of the system. Each set of subspaces represent each red point marked and labeled as 1, 2, 3 and 4 in Fig. 8. The associated equilibrium positions are displayed in each $\bar{z}_1 \times \bar{z}_2$ subspace for spatial reference. Poincaré maps are highlighted in red or black to indicate the type of dynamical response of the system

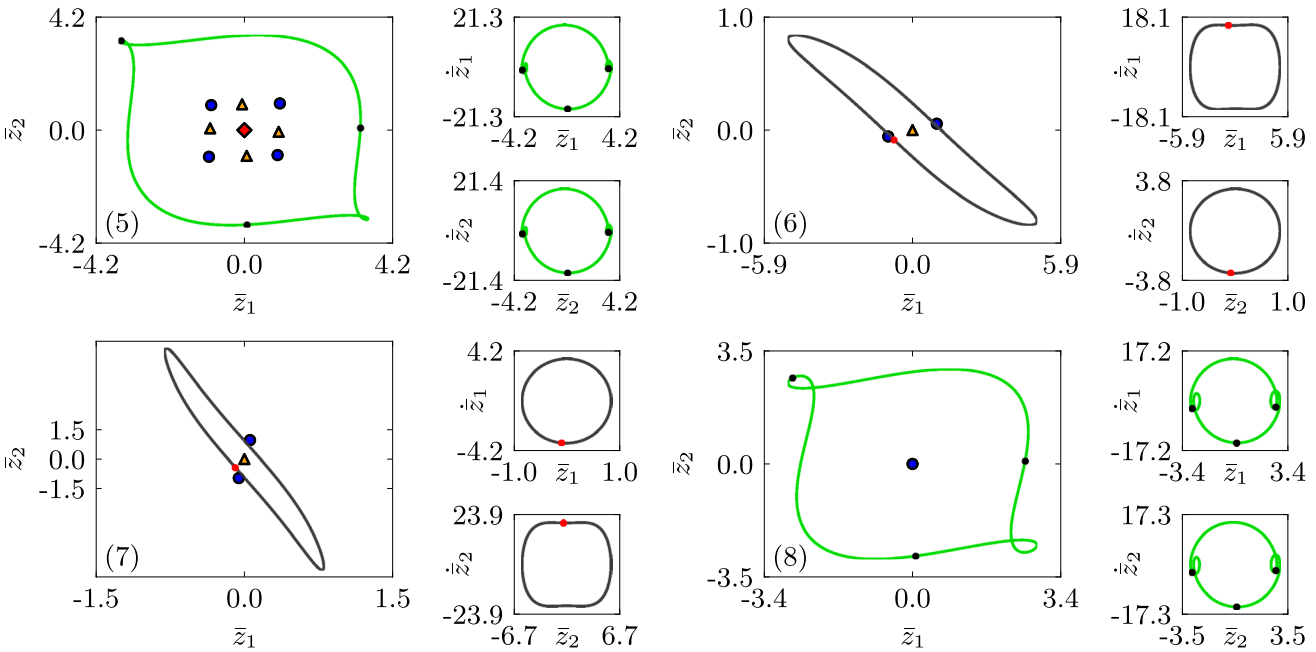

Fig. 10 Phase subspaces $\bar{z}_1 \times \bar{z}_2$, $\bar{z}_1 \times \dot{\bar{z}}_1$ and $\bar{z}_2 \times \dot{\bar{z}}_2$ of the steady state response of the system. Each set of subspaces represent each red point marked and labeled as 5, 6, 7 and 8 in Fig. 8. The associated equilibrium positions are displayed in each $\bar{z}_1 \times \bar{z}_2$ subspace for spatial reference. Poincaré maps are highlighted in red or black to indicate the type of dynamical response of the system

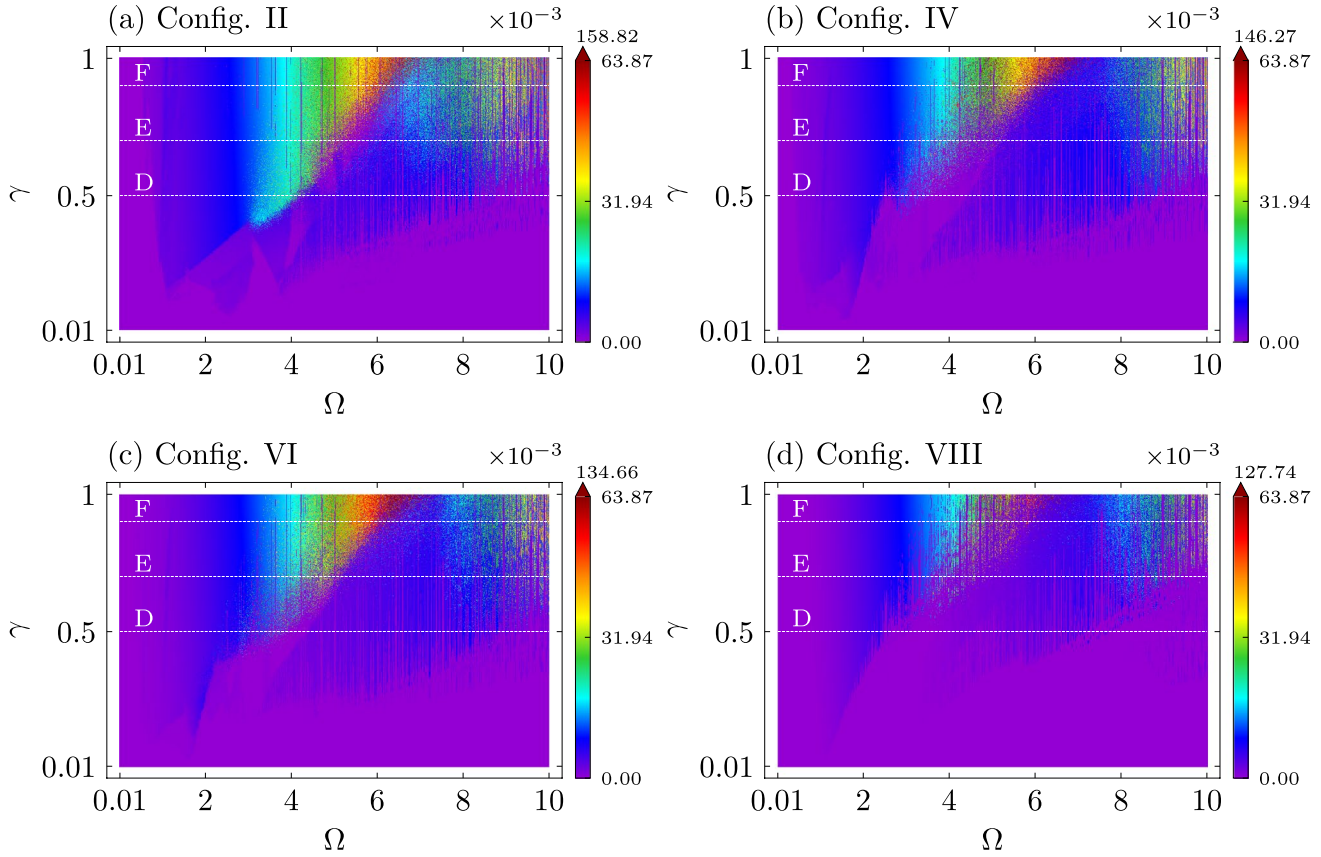

Fig. 11 Average output power diagrams (OPDs) for the configurations related to $\Omega_s = 1$. The colorbars represent the average output power levels for each excitation condition. To facilitate the interpretation, the range of each colorbar is restricted to a limit value, with the uppermost value of the colorbar on the peak of the colorbar arrow representing the maximum output power obtained by the harvester. All output power values are multiplied by 10^{-3}. White lines with capital letter labels are discussed in text and are represented by the frequency response diagrams in Fig. 12

output power, being determined as a region of poor performance. This characteristic holds true for all the configurations examined in this study, as showed in Figs. 7 and 11. Therefore, to focus on the significant excitation parameters, the subsequent OPDs are constrained to the range of $0.01 \leq \gamma \leq 0.5$ and $0.01 \leq \Omega \leq 5$. This region exhibits substantial output power for all configurations analyzed under low amplitude excitation scenarios ($\gamma \leq 0.5$).

Building upon the methodology employed in the previous subsection, Fig. 13 presents the OPDs for the configurations related to $\Omega_s = 0.25$. Subsequently, Fig. 14 further investigates the performance by focusing on specific constant values of γ. These values, marked by dashed lines within the OPDs, are identified as G ($\gamma \approx 0.03$), H ($\gamma \approx 0.1$), and I ($\gamma \approx 0.35$).

Overall, an overview of the OPDs points that configuration I offers superior overall performance compared to the other configurations. This is evident from the larger regions of high performance (represented by shades of red) observed in configuration I. In the same context, configuration III and V exhibit similar bandwidths, with configuration III displaying larger areas of high output power. Conversely, configuration VII exhibits the worst overall performance.

Yet, a careful analysis of very low excitation levels ($\gamma \leq 0.1$) is crucial, as many practical applications exhibit this characteristic. When considering such scenarios, configuration V and VII demonstrate better performance in terms of maximum output power; while, configurations III and V shows superior performance in terms of bandwidth. Surprisingly, configuration I displays the worst performance for these excitation levels. In contrast, by increasing the excitation levels, a significant shift occurs, leading to configuration I exhibiting improved overall performance; while, configuration VII shows the worst performance. Notably, the qualitative difference in performance remains consistent as γ increases. Figure 14 provides additional visual support for these findings through the frequency diagrams.

To deeply analyze this abrupt change in behavior, specific points in the vicinity of the maximum output powers

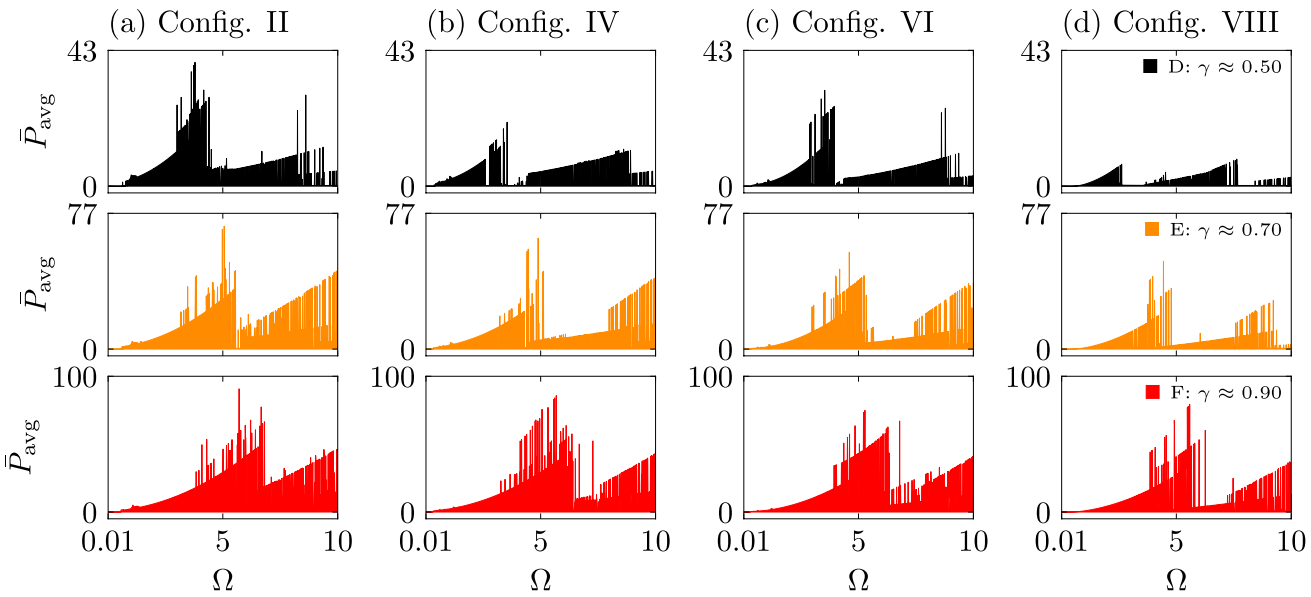

Fig. 12 Average output power for different values of constant γ. Each level of γ is highlighted by a different color: black for $\gamma \approx 0.5$, orange for $\gamma \approx 0.7$ and red for $\gamma \approx 0.9$. The constant values of γ are represented in Fig. 11 by the labels D, E and F. All average output power values are multiplied by 10^{-3}

within the frequency diagrams are carefully selected and highlighted in red. These points are labeled from 1 to 8. Figures 15 and 16 illustrate three phase subspaces ($\bar{z}_1 \times \bar{z}_2$, $\bar{z}_1 \times \dot{\bar{z}}_1$ and $\bar{z}_2 \times \dot{\bar{z}}_2$) of each selected point. Equilibrium points corresponding to each case in the $\bar{z}_1 \times \bar{z}_2$ phase subspaces are outlined for spatial reference. By comparing points 1 and 5, 2 and 6, 3 and 7, as well as 4 and 8 in Figs. 15 and 16, it becomes evident that the performance at very low γ is constrained by the potential energy barriers inherent of multistable systems. In the case of bistable and tetrastable configurations, the system remains trapped around a stable equilibrium position. As the system receives additional energy with increasing γ, it surpasses the potential barriers, leading to greater displacement and consequently improved performance. In this scenario, while the monostable configuration also experiences an increase in performance, it remains severely limited by the monostable potential. Additionally, in all subspaces, Poincaré maps are highlighted indicating the dynamical characteristics of the system, showing that enhanced performance are associated with higher displacement and complex phenomena, as indicating the orbits of periodicity 3T (green orbit), 5T (purple orbit), and chaotic (red orbit) in Fig. 16, where T is the excitation period. These observations shed light on the underlying mechanisms responsible for the observed behavior.

Figures 17 and 18, related to the configurations associated with $\Omega_s = 1$, exhibit a similar qualitative behavior, whereby the bistable configurations display poorest maximum output power for very low γ. As γ increases, there is a notable surge in performance attributed to the high amplitude response of the system, surpassing the energy barriers.

Still, a careful analysis of the OPDs in Fig. 17 reveals that configuration II demonstrates superior performance, characterized by larger regions of very high performance (depicted by shades of red). Nevertheless, for operation at lower frequencies ($\Omega \leq 1$), configurations IV and VI outperform configuration II, as they encompass regions of good performance (indicated by shades of blue); while, configuration II presents negligible performance (indicated by shades of purple). In contrast, configuration VIII, associated with monostability, exhibits by far the worst performance.

In general, this subsection demonstrates that for very low excitation levels, configurations VII and VIII, associated with monostability, yield higher output powers. On the other hand, configurations III, V, and IV exhibit superior bandwidths. For low to medium excitation levels ($0.1 \leq \gamma \leq 0.5$), configurations I and II exhibit better performances, while configurations VII and VIII consistently perform poorly.

4.3 Multiple solution regions

In Sect. 4.1, output power diagrams (OPDs) are presented for all configurations. Across all these diagrams, a distinctive region becomes evident when examining high-frequency and high-amplitude values. Within these zones, a non-smooth, irregular distribution of data points, showcasing a wide range of high and low output powers can be observed. This subsection is devoted to a comprehensive exploration of this

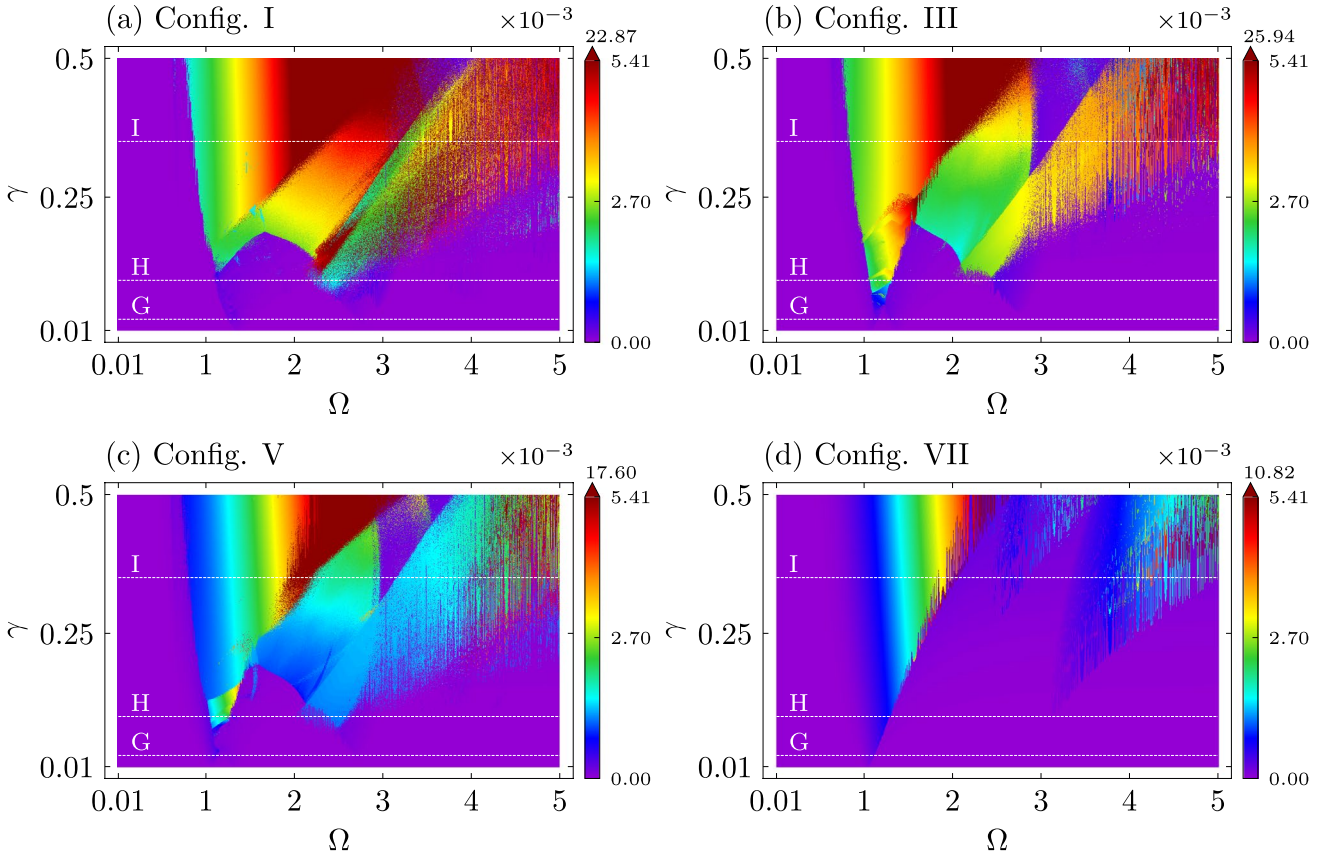

Fig. 13 Average output power diagrams (OPDs) for the configurations related to $\Omega_s = 0.25$. The colorbars represent the average output power levels for each excitation condition. To facilitate the interpretation, the range of each colorbar is restricted to a limit value, with the uppermost value of the colorbar on the peak of the colorbar arrow representing the maximum output power obtained by the harvester. All output power values are multiplied by 10^{-3}. White lines with capital letter labels are discussed in text and are represented by the frequency response diagrams in Fig. 14

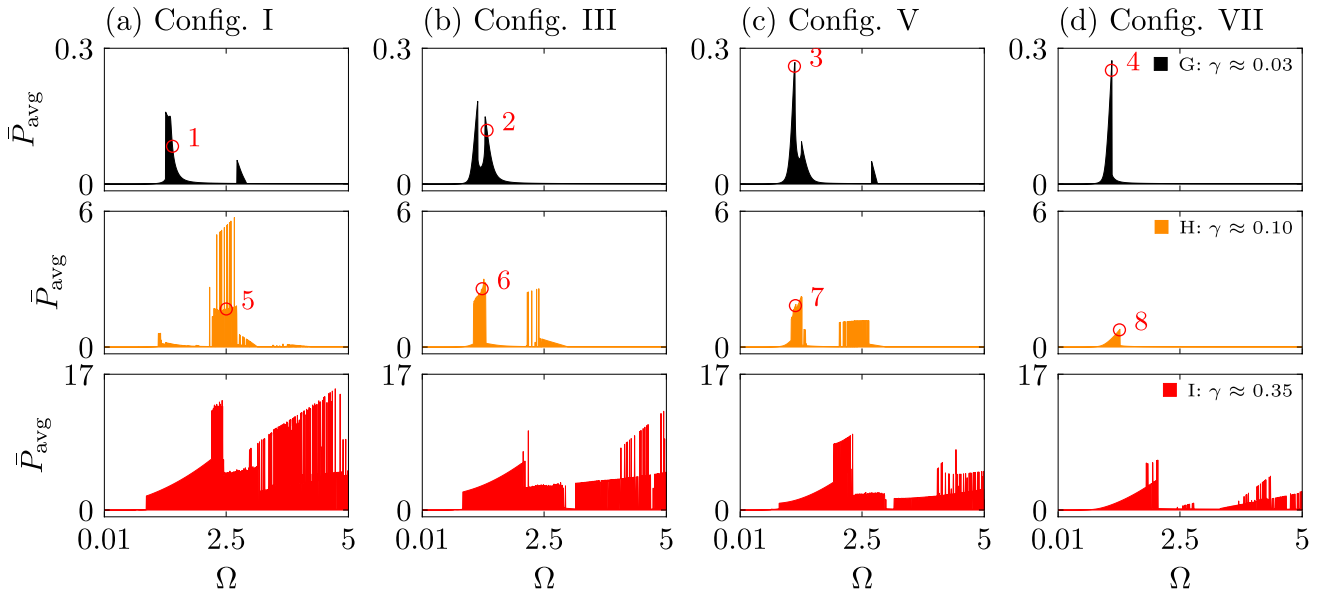

Fig. 14 Average output power for different values of constant γ. Each level of γ is highlighted by a different color: black for $\gamma \approx 0.03$, orange for $\gamma \approx 0.1$ and red for $\gamma \approx 0.35$. The constant values of γ are represented in Fig. 11 by the labels I, H and J. All average output power values are multiplied by 10^{-3}. Red points labeled with numbers are discussed in text and are represented by the phase spaces in Figs. 15 and 16

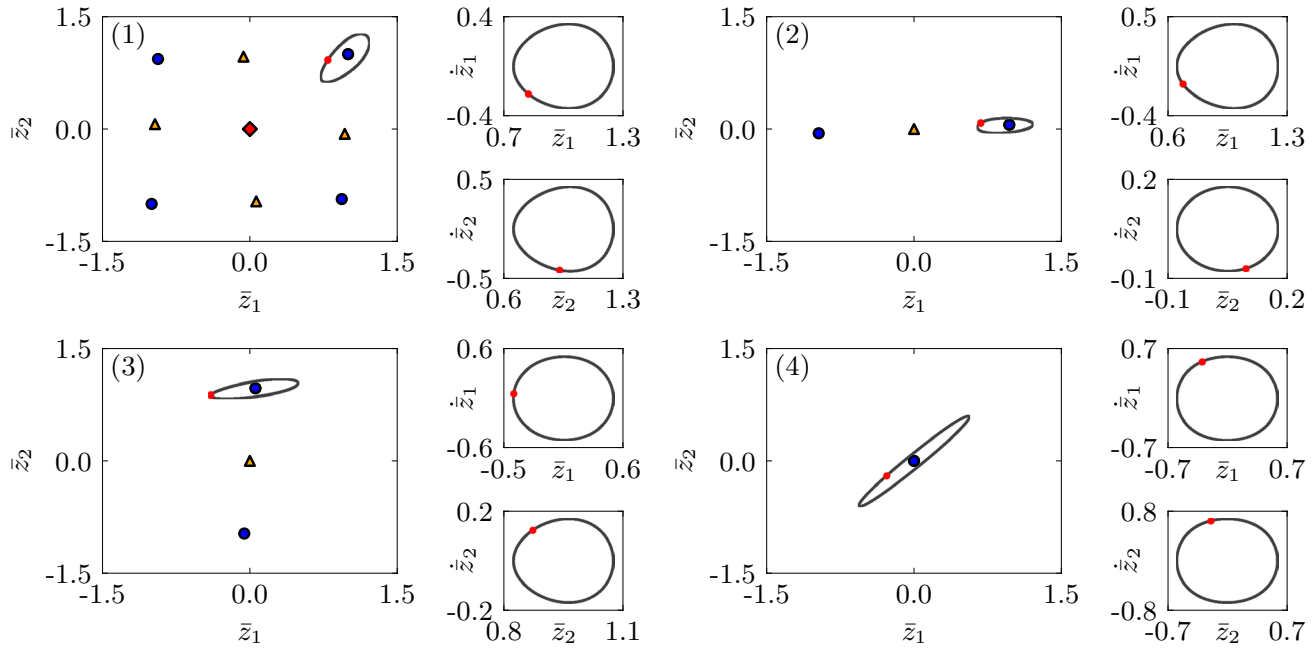

Fig. 15 Phase subspaces $\bar{z}_1 \times \bar{z}_2$, $\bar{z}_1 \times \dot{\bar{z}}_1$ and $\bar{z}_2 \times \dot{\bar{z}}_2$ of the steady state response of the system. Each set of subspaces represent each red point marked and labeled as 1, 2, 3 and 4 in Fig. 14. The associated equilibrium positions are displayed in each $\bar{z}_1 \times \bar{z}_2$ subspace for spatial reference. Poincaré maps are highlighted in red or black to indicate the type of dynamical response of the system

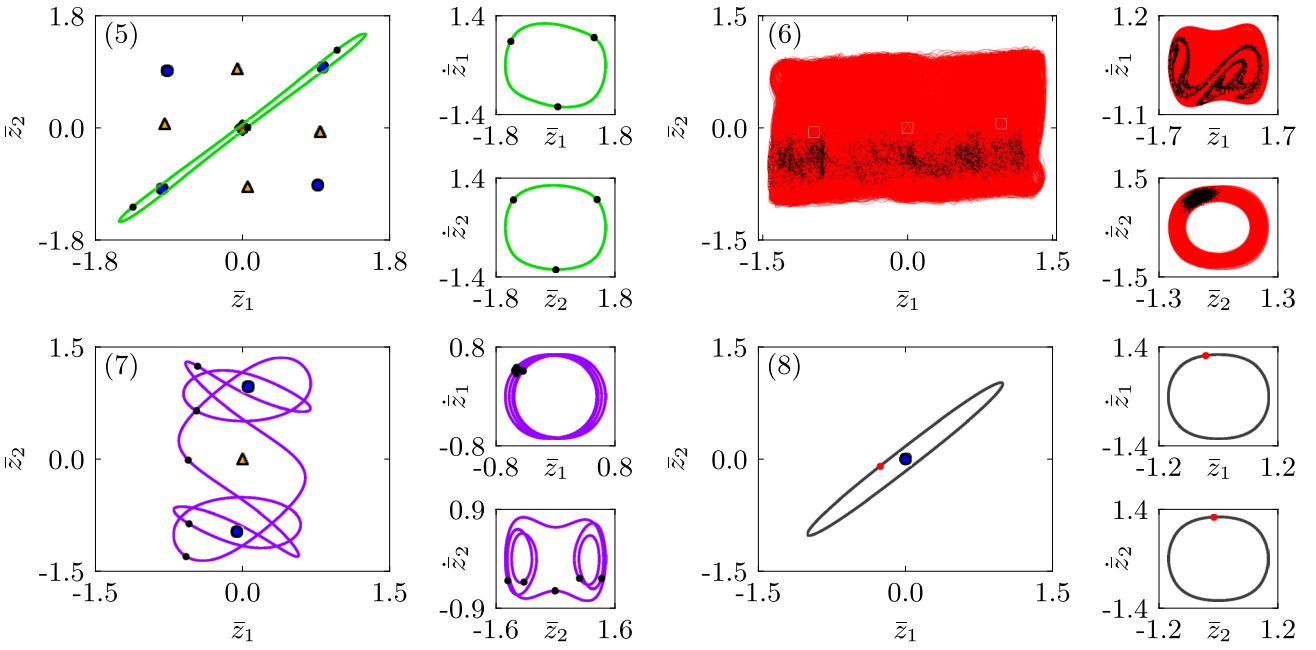

Fig. 16 Phase subspaces $\bar{z}_1 \times \bar{z}_2$, $\bar{z}_1 \times \dot{\bar{z}}_1$ and $\bar{z}_2 \times \dot{\bar{z}}_2$ of the steady state response of the system. Each set of subspaces represent each red point marked and labeled as 5, 6, 7 and 8 in Fig. 14. The associated equilibrium positions are displayed in each $\bar{z}_1 \times \bar{z}_2$ subspace for spatial reference. Poincaré maps are highlighted in red or black to indicate the type of dynamical response of the system

intriguing area, which from this point forward, is referred as the 'scattered zone'.

For that, consider Fig. 19 where the OPD for configuration I is selected. Here, a small region highlighted by the black dashed square and labeled as "PS" is chosen and,

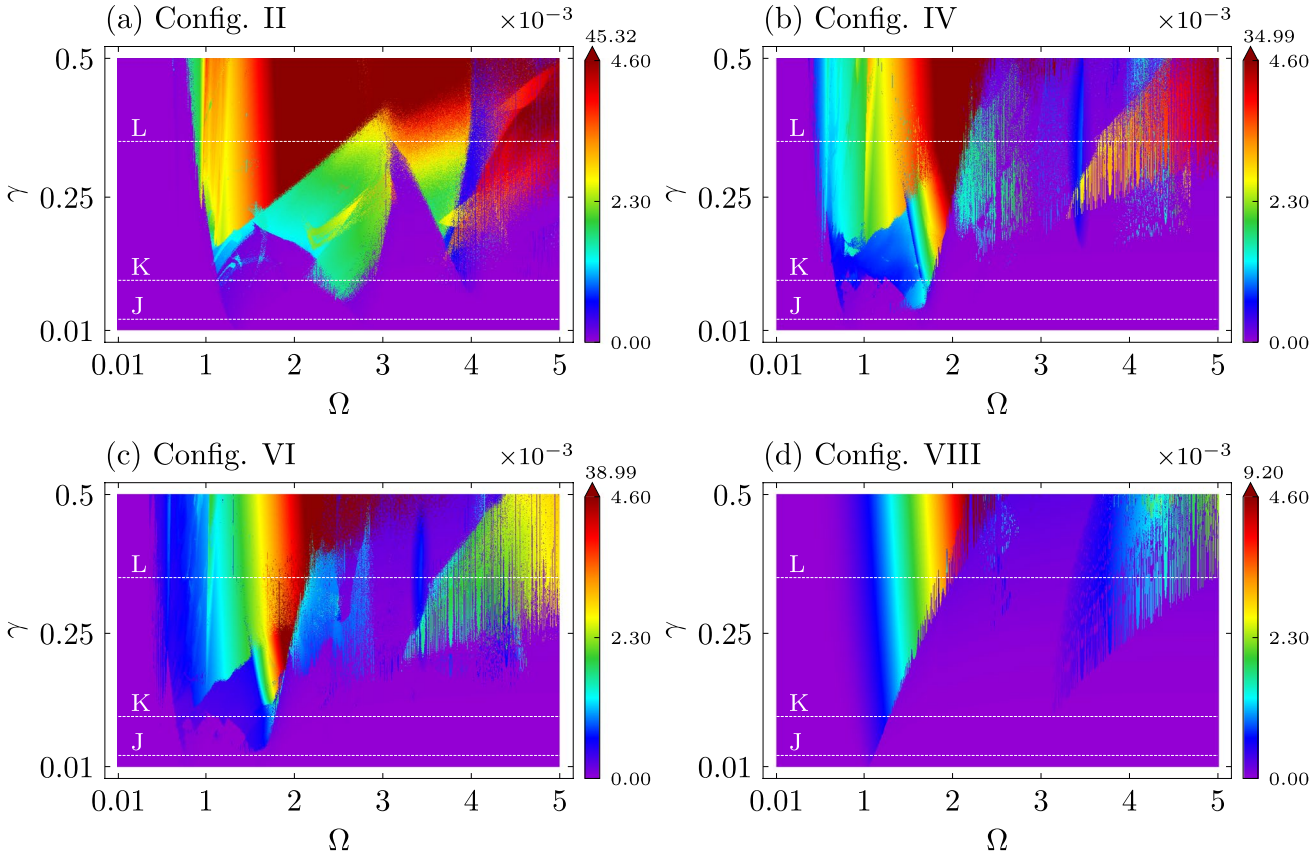

Fig. 17 Average output power diagrams (OPDs) for the configurations related to $\Omega_s = 1.00$. The colorbars represent the average output power levels for each excitation condition. To facilitate the interpretation, the range of each colorbar is restricted to a limit value, with the uppermost value of the colorbar on the peak of the colorbar arrow representing the maximum output power obtained by the harvester. All output power values are multiplied by 10^{-3}. White lines with capital letter labels are discussed in text and are represented by the frequency response diagrams in Fig. 18

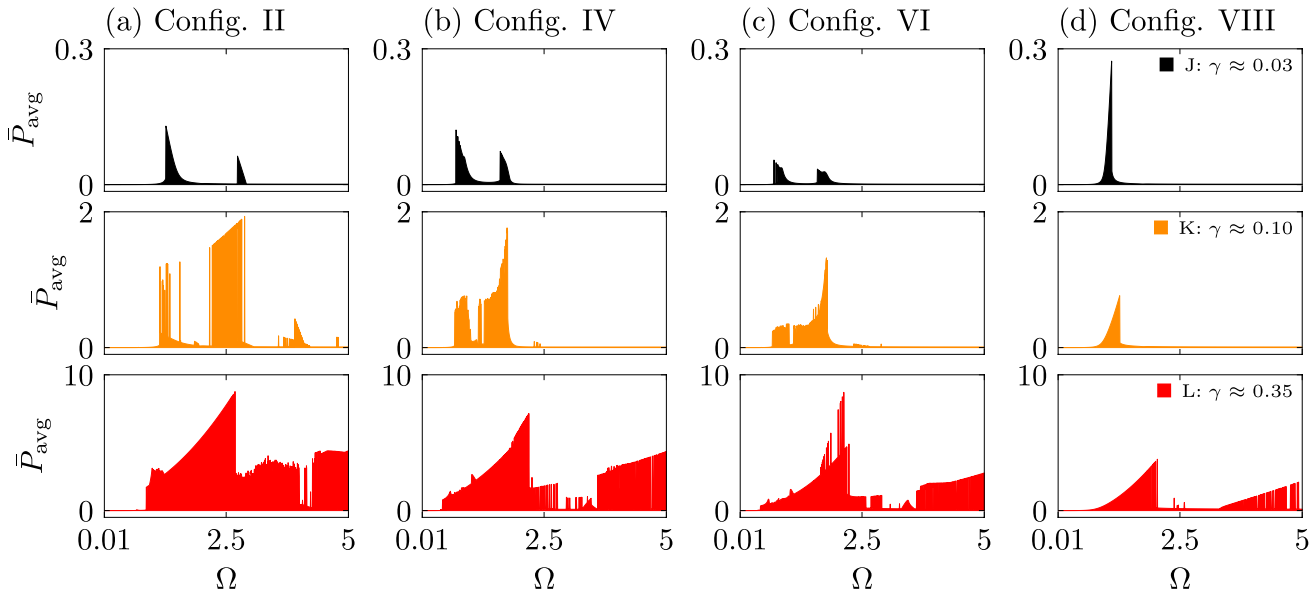

Fig. 18 Average output power for different values of constant γ. Each level of γ is highlighted by a different color: black for $\gamma \approx 0.03$, orange for $\gamma \approx 0.1$ and red for $\gamma \approx 0.35$. The constant values of γ are represented in Fig. 11 by the labels L, K and J. All average output power values are multiplied by 10^{-3}

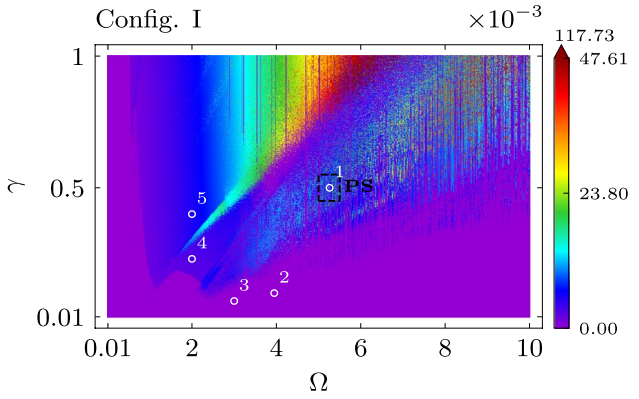

Fig. 19 Output power diagrams (OPD) for configuration I. The colorbars represent the average output power levels for each excitation condition. To facilitate the interpretation, the range of each colorbar is restricted to a limit value, with the uppermost value of the colorbar on the peak of the colorbar arrow representing the maximum output power obtained by the harvester. All output power values are multiplied by 10^{-3}. The black dashed rectangle region labeled as PS contains all the phase subspaces detailed in Fig. 20. Numbered white circles marks the locations of each basin of attraction displayed in Figs. 21 and 22

within this region, four very close points with $\gamma = 0.5$ and distinct values of Ω are chosen to be analyzed.

Figure 20 depicts the phase subspaces $\bar{z}_1 \times \bar{z}_2$, $\bar{z}_1 \times \dot{\bar{z}}_1$ and $\bar{z}_2 \times \dot{\bar{z}}_2$ of the steady state response of the chosen points within the black dashed rectangle. For each case, the average output power, $\bar{P}_{\text{avg}}$, is highlighted, showing that a small perturbation in excitation parameters can alter significantly the system's response, influencing its performance. In this case, four types of attractors are shown: 2 types of 3T attractors, a 9T attractor and a quasiperiodic-like attractor (T representing the period of excitation), each manifesting a distinct $\bar{P}_{\text{avg}}$.

Results presented in Fig. 20 suggest that the scattered zones are regions with many coexisting solutions. In order to confirm this hypothesis, consider an in-depth analysis of the basins of attraction of the forced system for the subspace $\bar{z}_1 \times \bar{z}_2$, as showcased in Figs. 21 and 22. This analysis categorizes the basins into two distinct types: those on the left, which exclusively consider attractors based on the system's motion characteristics; and those on the right, which also incorporate the impact of average output power.

The left-sided basins employ a classification methodology based on the steady state Poincaré maps and Lyapunov exponents, as detailed in Costa and Savi [5], to classify different types of dynamical attractors. These attractors are represented by a range of colors, each denoting different periodic or aperiodic behaviors. Dark gray corresponds to 1T periodic attractors, yellow to 2T attractors, green to 3T attractors, purple to 5T attractors, and light blue to multiple periods (MP), comprising all periodic attractors with a periodicity equals or greater than 6T. Additionally, red signifies chaotic (CH) attractors; while, dark red indicates hyperchaotic (HC) attractors. This classification is summarized in the colorbars next to the left-sided basins in each row.

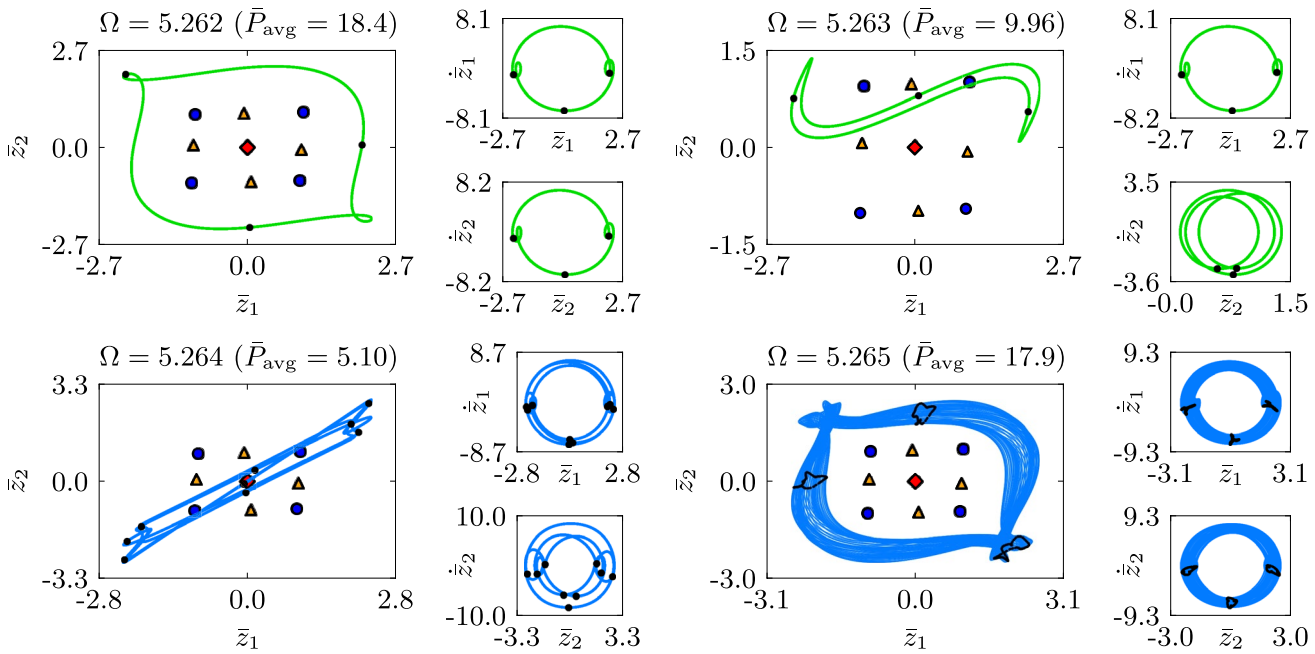

Fig. 20 Phase subspaces $\bar{z}_1 \times \bar{z}_2$, $\bar{z}_1 \times \dot{\bar{z}}_1$ and $\bar{z}_2 \times \dot{\bar{z}}_2$ of the steady state response of the system. Each set of subspaces represent a case with $\gamma = 0.5$ and a distinct Ω value within the PS zone highlighted in Fig. 19. The associated equilibrium positions are displayed in each $\bar{z}_1 \times \bar{z}_2$ subspace for spatial reference. Poincaré maps are highlighted in black to indicate the type of dynamical response of the system. Also the average output power, $\bar{P}_{\text{avg}}$, manifested in each response is highlighted

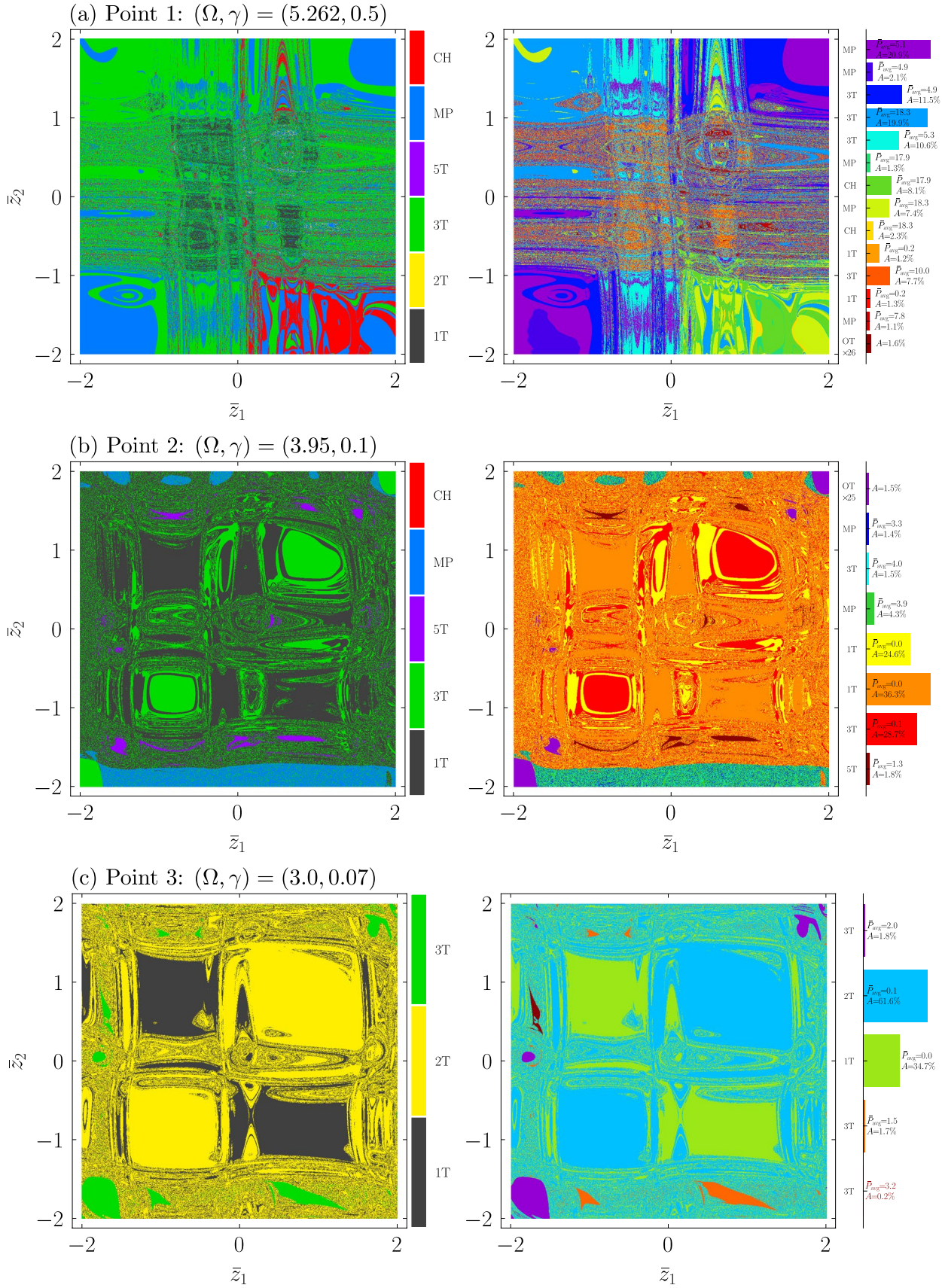
(a) Point 1: $(\Omega, \gamma) = (5.262, 0.5)$
(b) Point 2: $(\Omega, \gamma) = (3.95, 0.1)$
(c) Point 3: $(\Omega, \gamma) = (3.0, 0.07)$
$\bar{z}_1$
$\bar{z}_2$
CH
MP
5T
3T
2T
1T

◂**Fig. 21** Basins of attraction of the forced system for the subspace $\bar{z}_1 \times \bar{z}_2$: (a) Point 1, (b) Point 2, and (c) Point 3 (as highlighted in Fig. 19). The left-sided basins show the attractors related to the type of motion of the system, with each color of the colorbar representing one type of motion. The right-sided basins also incorporate the value of $\bar{P}_{\text{avg}}$ as a mean of classification, with the bar plot representing all the distinct motion–power attractors. Further details regarding the construction of the basins are discussed in text. A grid of 1000×1000 points is used

Furthermore, the right-sided basins employ a similar classification methodology, while also taking into consideration different values of $\bar{P}_{\text{avg}}$ to classify the attractors. To account for fluctuations and potential numerical errors associated with integration scheme, the classification considers intervals with a margin of approximately 2% around the $\bar{P}_{\text{avg}}$ values. In other words, when identifying a value of $\bar{P}_{\text{avg}}$, any values falling within a range of $\pm 2\%$ of the original value associated with a single periodic or aperiodic attractor are grouped as a unique motion–power attractor within this type of basin.

The motion–power attractors, which are based on the interplay of motion and power, are distinguished by various colors, as depicted in the horizontal bar plot adjacent to the right-sided basin. Additionally, the display includes information such as the type of motion, the $\bar{P}_{\text{avg}}$ value, and the area (A) occupied by the attractor within the basin. Moreover, when there are more than one attractor that occupies less than 1% of the basin area ($A < 1\%$), they are consolidated into a single color classification labeled as OT×N_{attr}, where 'OT' signifies 'other attractors,' and N_{attr} represents the number of attractors combined in this manner. If a specific attractor motion name replaces 'OT', it indicates that all consolidated attractors share the same type of motion.

Figure 21a presents the basins of attraction corresponding to the point 1, as indicated in Fig. 19, chosen to represent the scattered zone within the OPD. These basins reveal the potential for 39 distinct motion–power attractors to emerge depending on the displacement initial conditions, with 13 of them having a chance exceeding 1% to arise based on the occupied area. Among these 13 main attractors, four to five magnitudes of $\bar{P}_{\text{avg}}$ are observed. Furthermore, an examination of the basin morphology reveals that the most predictable responses originate from initial conditions situated at the corners of the plot. In these areas, the basin shapes are more consistent, and the values of $\bar{P}_{\text{avg}}$ are notably higher. Alternatively, the basin morphology near the stable equilibrium points are associated with an irregular fractal-like pattern, which can be associated with the unpredictability. These characteristics can be associated with the existence of the scattered zone in the OPDs, as they are built utilizing the a stable point as initial condition for all its points.

In a similar manner, Fig. 21b displays a case below the scattered zone, with still a mid-high Ω but with a lower γ. This region shows 32 motion–power attractors, with 7 of them occupying more than 1% of the plot area. Although this still represents a substantial number of attractors, it is fewer in comparison with point 1. The basin morphology, however, shows the opposite of the previous basin. In this case, the basin shapes near the equilibrium positions exhibit greater consistency, suggesting a higher degree of predictability; whereas, the surroundings of the plot are characterized by fractal-like patterns, which means a higher degree of unpredictability. Additionally, it is worth noting that in this case, the predictable zones with larger areas exhibit lower values of $\bar{P}_{\text{avg}}$, while the zones associated with unpredictability show higher performance.

Figure 21c shows the basin of the point 4 located in the OPD. In this case, the basins show characteristics that, in terms of output power and morphology, closely resemble those observed in the basin presented in Fig. 21b. Nevertheless, it implies that a significant reduction in the number of motion–power attractors can be achieved by reducing the frequency and amplitude of excitation. This reduction leads to an expansion of the overall area occupied by each attractor, enhancing the predictability of those with more consistent areas.

This hypothesis is strengthened by the basins presented in Fig. 22, that represents the points 4 and 5 highlighted in Fig. 19. These basins reveal that as the excitation frequency is decreased toward values closer to the linear natural frequency of the structure, a significant reduction in the number of attractors occurs. In point 5, there is only one attractor, while in point 4, there is virtually one. It is worth noting that the term 'virtually one' is used for point 4 because this basin reveals the presence of hyperchaotic responses, indicating that each point of the attractor represent a distinct, but similar response, in qualitative terms. This is supported by the right-sided basin which shows the classification of distinct hyperchaotic attractors with similar $\bar{P}_{\text{avg}}$ values and amorphous morphology of the basin. In these two instances, it becomes evident that the dynamical response and performance exhibit a remarkable level of predictability in point 4, and is 100% predictable in point 5.

Therefore, the scattered zone is a region with a high amount of coexisting solutions, which reduces the predictability of the system's performance. It seems that a control scheme is needed for the system to effectively operate within this region, ensuring good performance. Moreover, it is noticeable that the reducing of the frequency of excitation to a value near the linear natural frequencies can drastically improve its predictability. As a final point, the findings for Configuration I can be extrapolated for other configurations, however, further analyses of the remaining configurations must be carried out in order to be sure of that.

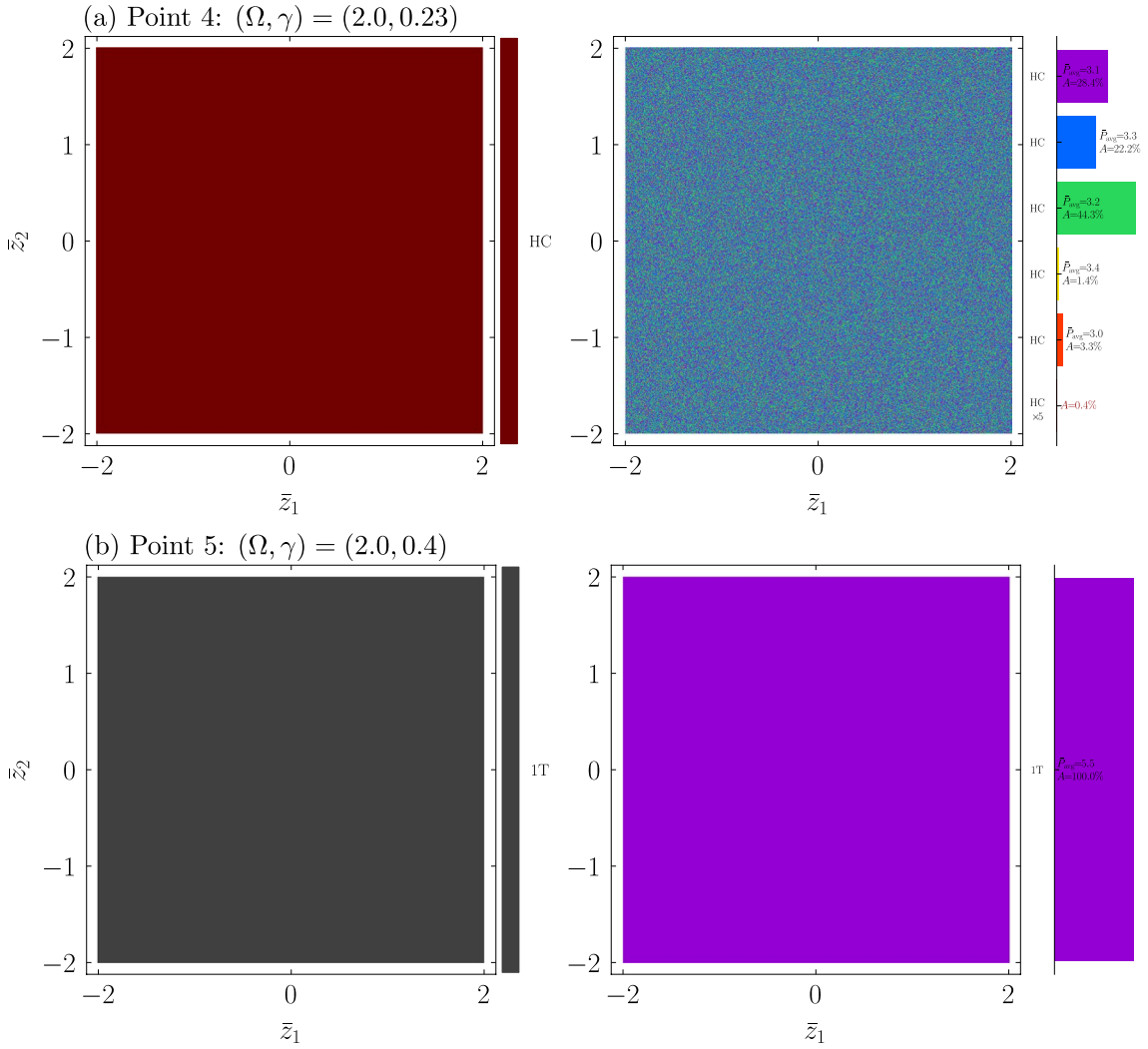

Fig. 22 Basins of attraction of the forced system for the subspace $\bar{z}_1 \times \bar{z}_2$: (a) Point 4 and (b) Point 5 (as highlighted in Fig. 19). The left-sided basins show the attractors related to the type of motion of the system, with each color of the colorbar representing one type of motion. The right-sided basins also incorporate the value of $\bar{P}_{\text{avg}}$ as a mean of classification, with the bar plot representing all the distinct motion–power attractors. Further details regarding the construction of the basins are discussed in text. A grid of 1000×1000 points is used in each plot

5 Conclusions

This investigation deals with a compact multistable nonlinear energy harvester proposed in Costa and Savi [5] to encompass various magnetic setups within the system. The harvester, designed to efficiently operate in restricted and compact spaces, is built upon classical structures using the cantilever beam as its foundation. By cutting off a section of the main beam, adding another in the inner part and incorporating a new set of magnets and transducer, the device exhibits multistability characteristics. A reduced order electromechanical model employing a two-degrees-of-freedom structure is chosen to represent the harvester and a qualitative investigation of the system is performed.

Stability analysis reveals that by considering different magnetic restitution parameters (α_1, α_2, β_1, β_2), the system can achieve tetrastability (with four stable equilibria), various forms of bistability (with two stable equilibria), and monostability (with one stable equilibria). Taking into account these differences, eight configurations are selected based on the magnetic setups for a comprehensive performance analysis. Additionally, the analysis is divided into two aspects to evaluate the system's performance under low and high excitation levels.

Results show that for very low excitation levels, monostable configurations yield higher output powers but inferior bandwidths compared with bistable configurations. Conversely, bistable configurations exhibit superior bandwidths but lower output power. Among the configurations,

the tetrastable configuration performs the poorest in this scenario. However, for low to high excitation levels, configurations I (tetrastable) and II (bistable) associated with magnetic parameters $(\alpha_1, \alpha_2, \beta_1, \beta_2) = (-2, -1, 1, 1)$ present superior performance in terms of maximum power output and bandwidth when compared to other configurations. The other bistable configurations exhibit similar performance when compared to each other. At very high excitation levels, the performance difference between bistable and tetrastable configurations reduces, as well as between monostable and bistable configurations. Nevertheless, all monostable configurations consistently underperform in scenarios with low to very high excitation levels. So, in general, configurations with smaller values of natural frequency ratio, Ω_s, present superior performance.

Furthermore, the observed variations in system behavior across these different scenarios are closely tied to the input energy levels. Tetrastable and bistable configurations exhibit potential energy barriers, which under low mechanical excitation levels, cannot be overcome due to insufficient energy, limiting the displacement of these systems and resulting in poor performance. As the system is powered with enough mechanical energy, the multistable characteristics enhance the displacement of the system and its complexity, resulting in enhanced performance. Moreover at high excitation levels, results indicate that the orbits demonstrating optimal performance consistently manifests as 1T attractors when occurring at intermediary frequency values and as 3T attractors when observed at higher frequency values. These attractors exhibit similar shapes.

Finally, the analysis of the basins of attraction for the forced system in configuration I highlights that operating under high-frequency and high-amplitude excitation conditions can result in the emergence of numerous coexisting solutions. In such scenarios, the predictability of the system's performance is reduced, emphasizing the imperative need of a control scheme to ensure good performance. Although this characteristic can be extrapolated for all configurations, further analyses of the remaining configurations must be carried out.

Acknowledgements The authors would like to acknowledge the support of the Brazilian Research Agencies CNPq (Conselho Nacional de Desenvolvimento Científico e Tecnológico), CAPES (Coordenação de Aperfeiçoamento de Pessoal de Nível Superior) and FAPERJ (Fundação Carlos Chagas Filho de Amparo à Pesquisa do Estado do Rio de Janeiro). The support of the AFOSR (Air Force Office of Scientific Research) is also acknowledged. Moreover, the authors also appreciate the use of the computational resources of the NACAD (Advanced High Performance Computing Nucleous).

Declarations

Conflict of interest The authors declare that they have no conflict of interest.

References

1. Bai Y, Jantunen H, Juuti J (2018) Hybrid, multi-source, and integrated energy harvesters. Fron Mater. https://doi.org/10.3389/fmats.2018.00065
2. Caetano VJ, Savi MA (2021) Multimodal pizza-shaped piezoelectric vibration-based energy harvesters. J Intell Mater Syst Struct 32:2505. https://doi.org/10.1177/1045389X211006910
3. Caetano VJ, Savi MA (2022) Star-shaped piezoelectric mechanical energy harvesters for multidirectional sources. Int J Mech Sci 215:106962. https://doi.org/10.1016/j.ijmecsci.2021.106962
4. Costa LG, da Silva Monteiro LL, Pacheco PMCL, Savi MA (2021) A parametric analysis of the nonlinear dynamics of bistable vibration-based piezoelectric energy harvesters. J Intell Mater Syst Struct 32:699. https://doi.org/10.1177/1045389X20963188
5. Costa LG, Savi MA (2023) Nonlinear dynamics of a compact and multistable mechanical energy harvester. Int J Mech Sci. https://doi.org/10.1016/j.ijmecsci.2023.108731
6. De Paula AS, Inman DJ, Savi MA (2015) Energy harvesting in a nonlinear piezomagnetoelastic beam subjected to random excitation. Mech Syst Signal Process 54–55:405. https://doi.org/10.1016/j.ymssp.2014.08.020
7. Deng Z, Dapino MJ (2015) Modeling and design of Galfenol unimorph energy harvesters. Smart Mater Struct 24:125019. https://doi.org/10.1088/0964-1726/24/12/125019
8. Erturk A, Hoffmann J, Inman DJ (2009) A piezomagnetoelastic structure for broadband vibration energy harvesting. Appl Phys Lett 94:254102. https://doi.org/10.1063/1.3159815
9. Erturk A, Inman D (2011) Broadband piezoelectric power generation on high-energy orbits of the bistable duffing oscillator with electromechanical coupling. J Sound Vib 330:2339. https://doi.org/10.1016/j.jsv.2010.11.018
10. Erturk A, Inman DJ (2009) An experimentally validated bimorph cantilever model for piezoelectric energy harvesting from base excitations. Smart Mater Struct 18:025009. https://doi.org/10.1088/0964-1726/18/2/025009
11. IEA (2021) Renewables 2021—analysis and forecast to 2026. In: Technical report. International Energy Agency - IEA, Paris. https://www.iea.org/reports/renewables-2021
12. Iqbal M, Nauman MM, Khan FU et al (2021) Vibration-based piezoelectric, electromagnetic, and hybrid energy harvesters for microsystems applications: a contributed review. Int J Energy Res 45:65. https://doi.org/10.1002/er.5643
13. Jiang J, Liu S, Feng L, Zhao D (2021) A review of piezoelectric vibration energy harvesting with magnetic coupling based on different structural characteristics. Micromachines. https://doi.org/10.3390/mi12040436
14. Kim JE, Kim YY (2011) Analysis of piezoelectric energy harvesters of a moderate aspect ratio with a distributed tip mass. J Vib Acoust. https://doi.org/10.1115/1.4003598
15. Kim M, Hoegen M, Dugundji J, Wardle BL (2010) Modeling and experimental verification of proof mass effects on vibration energy harvester performance. Smart Mater Struct 19:045023. https://doi.org/10.1088/0964-1726/19/4/045023
16. Kumar KA, Ali SF, Arockiarajan A (2015) Piezomagnetoelastic broadband energy harvester: nonlinear modeling and characterization. Eur Phys J Spec Top 224:2803. https://doi.org/10.1140/epjst/e2015-02590-8
17. Lallart M, Zhou S, Yan L, Yang Z, Chen Y (2019) Tailoring multistable vibrational energy harvesters for enhanced performance: theory and numerical investigation. Nonlinear Dynam 96:1283. https://doi.org/10.1007/s11071-019-04853-6
18. Masana R, Daqaq MF (2010) Electromechanical modeling and nonlinear analysis of axially loaded energy harvesters. J Vib Acoust. https://doi.org/10.1115/1.4002786

19. Ou Q, Chen X, Gutschmidt S et al (2012) An experimentally validated double-mass piezoelectric cantilever model for broadband vibration-based energy harvesting. J Intell Mater Syst Struct 23:117. https://doi.org/10.1177/1045389X11431746
20. Rezaei M, Talebitooti R, Liao W-H (2021) Exploiting bi-stable magneto-piezoelastic absorber for simultaneous energy harvesting and vibration mitigation. Int J Mech Sci 207:106618. https://doi.org/10.1016/j.ijmecsci.2021.106618
21. Safaei M, Sodano HA, Anton SR (2019) A review of energy harvesting using piezoelectric materials: state-of-the-art a decade later (2008–2018). Smart Mater Struct 28:113001. https://doi.org/10.1088/1361-665X/ab36e4
22. Savi MA (2017) Dinâmica Não-Linear e Caos, 2nd edn. E-papers, Brazil
23. Sneller AJ, Cette P, Mann BP (2011) Experimental investigation of a post-buckled piezoelectric beam with an attached central mass used to harvest energy. Proc Inst Mech Eng Part I J Syst Control Eng 225:497. https://doi.org/10.1177/0959651811401954
24. Stanton SC, McGehee CC, Mann BP (2009) Reversible hysteresis for broadband magnetopiezoelastic energy harvesting. Appl Phys Lett 95:174103. https://doi.org/10.1063/1.3253710
25. Steffen W, Rockström J, Richardson K et al (2018) Trajectories of the earth system in the Anthropocene. Proc Natl Acad Sci 115:8252. https://doi.org/10.1073/pnas.1810141115
26. Sukumaran S, Chatbouri S, Rouxel D et al (2021) Recent advances in flexible PVDF based piezoelectric polymer devices for energy harvesting applications. J Intell Mater Syst Struct 32:746. https://doi.org/10.1177/1045389X20966058
27. Tan Y, Dong Y, Wang X (2017) Review of MEMS electromagnetic vibration energy harvester. J Microelectromech Syst 26:1. https://doi.org/10.1109/JMEMS.2016.2611677
28. Wang C, Song Z, Gao Z, Yu G, Wang S (2019) Preparation and performance research of stacked piezoelectric energy-harvesting units for pavements. Energy Build 183:581. https://doi.org/10.1016/j.enbuild.2018.11.042
29. Wu H, Tang L, Yang Y, Soh CK (2013) A novel two-degrees-of-freedom piezoelectric energy harvester. J Intell Mater Syst Struct 24:357. https://doi.org/10.1177/1045389X12457254
30. Wu H, Tang L, Yang Y, Soh CK (2014) Development of a broadband nonlinear two-degree-of-freedom piezoelectric energy harvester. J Intell Mater Syst Struct 25:1875. https://doi.org/10.1177/1045389X14541494
31. Zhou W, Wang B, Lim C, Yang Z (2021) A distributed-parameter electromechanical coupling model for a segmented arc-shaped piezoelectric energy harvester. Mech Syst Signal Process 146:107005. https://doi.org/10.1016/j.ymssp.2020.107005
32. Zhou Z, Qin W, Yang Y, Zhu P (2017) Improving efficiency of energy harvesting by a novel penta-stable configuration. Sens Actuators A Phys 265:297. https://doi.org/10.1016/j.sna.2017.08.039
33. Zhou Z, Qin W, Zhu P (2017) A broadband quad-stable energy harvester and its advantages over bi-stable harvester: simulation and experiment verification. Mech Syst Signal Process 84:158. https://doi.org/10.1016/j.ymssp.2016.07.001
34. Zhu G, Peng B, Chen J, Jing Q, Lin Wang Z (2015) Triboelectric nanogenerators as a new energy technology: from fundamentals, devices, to applications. Nano Energy 14:126. https://doi.org/10.1016/j.nanoen.2014.11.050
35. Zhu J, Liu X, Shi Q et al (2020) Development trends and perspectives of future sensors and MEMS/NEMS. Micromachines. https://doi.org/10.3390/mi11010007
36. Zou H-X, Zhao L-C, Gao Q-H et al (2019) Mechanical modulations for enhancing energy harvesting: principles, methods and applications. Appl Energy 255:113871. https://doi.org/10.1016/j.apenergy.2019.113871